2020

A Four-Port Bidirectional DC-DC Converter for Renewable Energy System and Microgrid

Xia Du
Minnesota State University, Mankato

A FOUR-PORT BIDIRECTIONAL DC-DC CONVERTER FOR RENEWABLE ENERGY SYSTEM AND MICROGRID

By

Xia Du

A Thesis Submitted in Partial Fulfillment of the

Requirements for the Degree of

Master of Science

In

Electrical Engineering

Minnesota State University, Mankato

Mankato, Minnesota

July, 2020

July 10, 2020

A four-port bidirectional DC-DC converter for renewable energy system and microgrid,

Xia Du

This thesis has been examined and approved by the following members of the student's committee.

_____
Advisor

_____
Committee Member

_____
Committee Member

A FOUR-PORT BIDIRECTIONAL DC-DC CONVERTER FOR RENEWABLE ENERGY SYSTEM AND MICROGRID

Xia Du

Advisor: Jianwu Zeng

MINNESOTA STATE UNIVERSITY, MANKATO

MANKATO, MINNESOTA

July, 2020

ABSTRACT

Renewable energy has nowadays become important in electrical power applications. Power converters play an important role in integrating these distributed energy sources. However, due to their intermittence characteristics, e.g., the output power provided by the PV and wind turbine is not stable, either an energy storage system will be used or microgrid is formed between the main grid and the sources. To integrate these renewable energy sources and manage the power flow, a multiport converter is preferred because it is highly beneficial and cost efficiently than traditional solutions that using multiple individual power converter for each source.

This thesis proposed a novel four-port bidirectional DC-DC converter with a battery storage system, which uses phase-shift control of two active bridges connected through two transformers. Compared with the traditional multiport converters, the proposed four-port converter uses the least number of power switches and zero-voltage switching (ZVS) for all the switches can be realized. The design and effectiveness of controllers are validated by experimental results. The converter can work in different scenarios regardless the availability of the renewable energy and the state-of-charge of the battery. In addition, maximum power point tracking for renewable energy sources can be achieved for each renewable energy source while managing the power flow of the battery.

ACKNOWLEDGMENTS

Entering into the research era of power electronics, I have experienced a bumpy process from theory to practice. However, I felt a glow of pride that I have chosen this research team and achieved a qualitative change from a student to a researcher with all your help. Firstly, I would like to say special thank you to my supervisor, Dr. Jianwu Zeng, who continuously provided encouragement and was always willing and enthusiastic to assist in any way he could throughout the research project. His support, guidance and overall insights in this field have made this an inspiring experience for me. In addition, I am extremely grateful for all the research group members for their energy, understanding and help throughout my project, it truly has been very good time in this lab. I also would like to say thank you to my committee members, Dr. Winstead and Dr. Qiang Ye, for their advice and research tips.

Financial support from the Xcel Energy through a grant from the Renewable Development Fund is gratefully acknowledged. I am also thankful to the School of Engineering and all its member's staff for all the considerate guidance. To conclude, I cannot forget to thank my family and friends for all the unconditional support in this very intense academic year.

TABLE OF CONTENTS

LIST OF TABLES

Chapter 1 : Introduction and background

1.1 Introduction

With the increasing concern in renewable energy sources (RESs) due to their important role they play in the environmental, sustainable and affordable power systems, more and more countries accept and manage to develop RESs since they can take the place of the traditional fossil fuels to defuse the energy crisis. In addition, RESs can curb the carbon emission to have a good effect in climate change [1]. Over the years, the most exploited and promising RESs are photovoltaic (PV) and wind. As the technology matures in PV systems and wind turbines, the advantageous complementarities between solar energy and wind energy are a common occurrence in the power system [2]. Although the benefits of using RESs are considerable, how to integrate them effectively to serve people is still a big challenge because of their operating characteristics such as lower and more variable capacity factors and variable, intermittent availability [3].

To solve the problems mentioned above, DC-DC converters are developed to integrate different power supplies to the load, which have been widely used in Microgrids [4]. There are two ways to design the converters: 1) Conventional DC-DC converter which can only be connected with one source of energy; 2) Multiport DC-DC converter which can interface several renewable power sources such as wind, solar energy systems and realize the power management. Fig. 1.1 shows the two kinds of DC-DC converters. Fig. 1.1 (*a*) is the conventional DC-DC converter, Fig. 1.1 (*b*) is known as a three ports converter: it can be seen that the power supplies are connected to two sources PV and wind

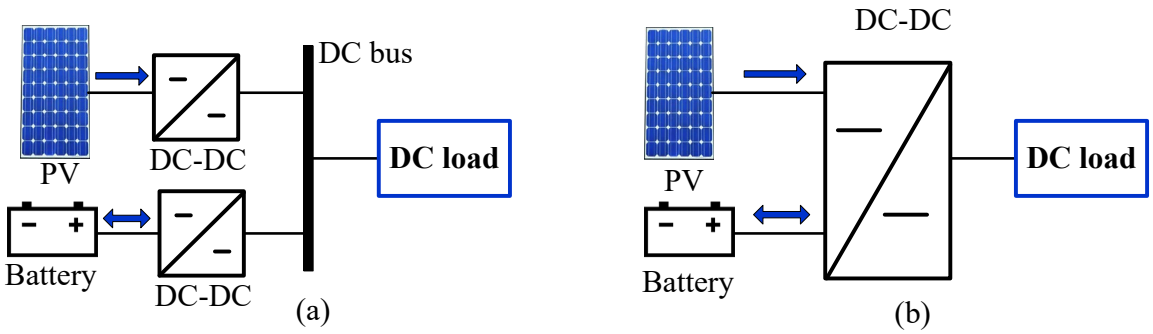

Fig. 1.1 Converter systems: (*a*) Traditional system; (*b*) multiport system.

turbine while the other side is connected to the load. Obviously, the latter one contributes to reduce the system cost and volume.

1.2 Introduction to Renewable Energy Conversion and Energy Storage Systems

1.2.1 Wind Energy Conversion System

Wind energy is a significant component of the modern and future energy supply systems with the cumulative installation of wind turbines over the last two decades [5]. Along with the fast-growing capacity and the fast evolution of power electronics, wind energy conversion system (WECS) has matured to a level of development where it is ready to become a generally accepted utility generation technology [6]. The initial design of the wind turbine generator (WTG) is the squirrel-cage induction generator (SCIG) which has

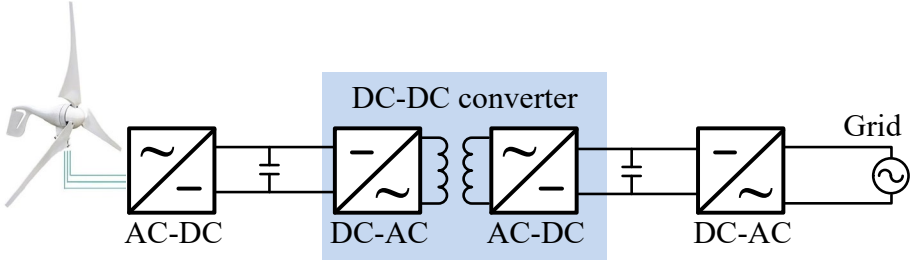

Fig. 1.2 WECS concept with full-scale power converter.

the fixed rotational speed, thus the WTG cannot achieve its maximum efficiency in a constantly changing wind speeds situation, and thereby has reduced energy generated. To satisfy growing demands for wind energy supplement, wound-rotor induction generators (WRIGs) were developed in the 1990s, which could work at a limited range of the rotational speed. Since 2000s, more and more advanced power converters with bidirectional power flow have been developed, which has brought significant performance improvements to current wind power technology, such as Variable-Speed Wind Turbines [7]- [8].

Fig. 1.2 shows the current wind turbine concept. There are a lot advantages to use the current wind turbine technology: reducing mechanical stress, generating more energy and enabling the WTGs to act as a controllable generator which are much more suitable for integration with the power grid. However, how to increase the efficiency of the WECS and improve the transmission technology in the future are need to be solved.

1.2.2 PV System

The National Renewable Energy Laboratory (NREL) published a variety of documents related to solar market and Cost-Reduction Roadmap for Residential Solar Photovoltaics 2017-2030, which shown that the residential PV market has great potential, and an estimation annually 3.3 million homes will be built or require roof replacement, representing a residential PV technical potential of roughly 30 GW per year [9]-[10]. As PV systems have become cheaper and prevalent every year, this rapid development of the solar energy is expected to continue in the future and will be driven by innovations particularly in efficiency and reliability.

The rapid development of the converters contributes to fulfill the amazing potential of the solar energy to power our daily lives. At present, there are two major categories of the photovoltaic power system: one-stage and two-stage PV system [11]. For the one-stage PV system, the solar energy generated by the solar panels is converted to standard DC voltage, e.g., 180 V, through the converter to supply load directly as shown in Fig. 1.3 (*a*). For the two-stage PV system, the solar energy is converted into standard sinusoidal AC current through the inverter to the load or grid as shown in Fig. 1.3 (*b*). Normally, a power system will be connected to the main grid for most of the time, known as the grid-connected mode. Otherwise, it is the stand-alone mode. In this thesis, the PV system will be connected to a DC-DC converter to regulate the output voltage and work in the high efficacy mode by implementing the maximum power point tracking (MPPT) technique.

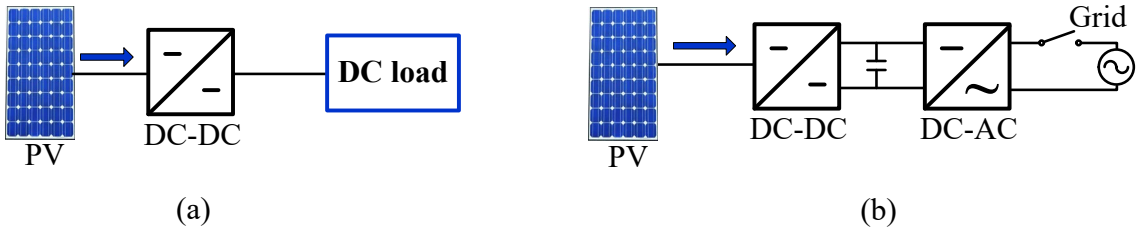

Fig. 1.3 PV system: (a) stand-alone system; (b) Grid connected system.

1.2.3 Energy Storage Systems

The whole world is in great need of energy system [12], e.g., manufacturing, service industry, all the portable electronics to the renewable energy industry. Especially, solar, PV generation and electric vehicle (EV) have made great strides in worldwide, thus energy storage systems (EESs) are becoming more and more important. As aforementioned intermittence characteristics of the RESs, EES is desired to smooth out the supply across

the day by storing energy converted from RESs at times of low demand and releasing during peaks.

Batteries are commonly used for storing electrical energy, ranging in size from the button cells used in watches to megawatt load leveling applications. Batteries fall into two broad classifications: electrochemical batteries and fuel cells. Fuel cells operating on liquid fuels such as methanol are described as primary batteries since they are not normally rechargeable and must be refilled before they are used up, therefore, they are not applicable for repetitively storing energy. For electrochemical batteries, such as Lead–Acid batteries, Li-oxygen batteries, they can have high energy storage but their output power is limited [13] .

However, the lithium-ion battery has been proven to have excellent performance in portable electronics and grid storage even thorough there is still much room for improvement [14] - [17]. In terms of the high-output voltages, high-energy densities, low memory effect, and good high-temperature performance, the lithium-ion battery makes a good substitute for other types of batteries. Moreover, its long cycle life, rate capability, long-term stability, safety, and low cost have enabled Li-ion technology to make in-roads in both automotive and grid applications.

1.3 Background of Renewable Energy Integration to the Microgrid

1.3.1 Microgrid with RESs

A smart grid is an electricity network which includes a variety of operation of its interconnected elements from energy measures including smart meters, smart appliances, and all generation sources such as renewable energy resources, to end-use consumers [18].

The smart grid is considered to be the next-generation power system that will significantly enhance the efficiency and reliability of the power grid, particularly with the integration of RESs and demand response. The utilization of emerging/intelligent devices and the digital technology improving communications makes the grid smart.

Microgrids are of a smaller scale of the smart grid and generally treated as a single controllable entity, which is composed of a central controller and a group of localized electrical consumers (or users) equipped with RESs and energy storages as shown in Fig. 1.4.

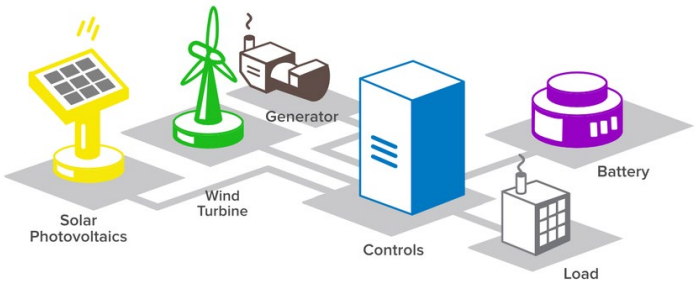

Fig. 1.4 A schematic of a Macrogrid [19].

Microgrids can either work as islanded mode or grid-connected mode. A grid-connected mode is one that the local utility grid works in connected to the main grid so that when RESs produce more solar electricity than the load is using the surplus power is fed into the grid. An islanded mode is not connected to the main grid, the local sources must undertake the job of catering to the loads. Renewable energy technology such as PV panel is suitable in microgrids application because its clean and the inherent intermittency of renewable power can be mitigated with dispatchable units like micro-turbines and battery banks [20]. According to the conversion stage, there are two solutions to integrate RESs

based on the macrogrids: a one-stage DC-AC system and a two-stage DC-DC-AC system. This thesis will focus on the latter one.

1.3.2 Two-Stage DC-DC-AC Power Conversion System

Hybrid dc/ac power systems with renewable energy sources such as solar and wind energy are receiving increasing weight in research because of the urgent demand for renewable energy and the rapid development of high penetration of technologies, i.e. photovoltaic (PV), wind turbine, energy storage systems, and microgrids. Solar energy which is strongly affected by the weather condition, area or seasonal change generally requires DC-DC conversion system to regulate the voltage, so does the wind energy. Therefore, DC-DC converters used as an interface for the solar panel and wind turbine are regarded as the first stage. To achieve the power management, the energy storage system and the load has been widely investigated. The process of realizing DC to AC is considered as the second stage. Most of these converters consist of more than one stage, i.e. DC-AC or DC-DC-AC converters that each one has its own power semiconductor switches.

Two-stage grid connected power conversion system, containing a front-end DC-DC converter followed by a DC-AC Inverter, has been widely studied because of its wide input voltage range and simple control method. However, there are still a lot of challenges, like the big size and use too many components, which results in more expensive and lower reliability compared to one stage topologies. So the development of one stage topologies are encouraged more in recent years to improve the efficiency by reducing the power conversion stage [21].

1.4 Review of Prior and Related Work

According to the topology of the converters, the DC-DC converters can be configured into two types: isolated and non-isolated converters [22]. Isolation is the physical and electrical separation between one section of a circuit and another, which is achieved generally by using transformers. Thus each of the isolated circuits has its own return or ground reference. A non-isolated power converter has a single circuit in which current can flow between the input and output. So far, a lot of investigations related to isolated multiport converters have been reported [23] - [27], which can be used to break up ground loops, shift or invert the output relative to another point in a circuit and satisfy safety requirements. Only few non-isolated converters have been proposed [28], which have a smaller size, better efficiency, and lower cost compared to the isolated converters. Choosing which type converters depends on many factors, understanding the costs and benefits of isolation is important in choosing the right converter for an optimized design.

For the standalone multiport converters, which are connected to the renewable energy sources and battery as backup. The battery can be charged by the redundant renewable energy, and discharged to supply power to the load when the renewable energy is insufficient. For the grid-connected multiport converters, the excessive energy of the grid or the redundant renewable energy both can be transferred to the battery to store energy for backup, which can realize the bidirectional power flow. Therefore, bidirectional converters play a crucial role in the power management. Fortunately, the bidirectional technique has been fully developed in many topologies.

All the multiport converters proposed above are three ports, so increasing the port, improving the efficiency and realizing the smart power management still is a big challenge. Meanwhile, coordinating the transfers of renewable energy between the battery and grid is particularly difficult due to the stochastic nature of renewable energy, and the dynamic energy demand of each user.

1.5 Research Objectives

Inspired by the fact that the rapidly evolving semiconductor switches are widely used in the cost-effective and grid-friendly converters, handling high power, high efficiency are becoming the new pursuit in the integration of the renewable energy systems. Meanwhile, the advanced real-time controllers make great ideas a reality: the unstable voltage and current can be smoothly converted into smart grid, and the hybrid energy can coordinate their power supplement without human intervention. These can be achieved by the following three objectives.

1) Improve of the efficiency. The power conversion loss of a converter is mainly caused by the semiconductor devices and magnetic components of the converter. To increase the overall efficiency of the converter, soft-switching techniques, such as zero-voltage switching (ZVS) and zero-current switching (ZCS), are desired. In addition, the design of the converters should minimize the number of power semiconductor devices.

2) Realize bidirectional power flow. In grid-connected mode, the management of directional power flow is used to store extra energy as backup, which can not only balance the power between the generation and the load, but also improve energy efficiency in an indirect way.

3) Guarantee the system to work stable in different dynamic modes. The controllers are design to control the voltage of DC link to 180V, the maximum voltage of battery to 30V as a protection. Most importantly, the dynamic response should be quick, accurate and reliable.

1.6 Outline of Thesis

Following the above introductions, an outline of this dissertation is given as follows.

Chapter 2 proposes a novel bidirectional four-port DC-DC converters for a hybrid wind, solar, and battery system. The topology, operating principles, ZVS analysis and the control strategy of the power management are discussed.

Chapter 3 presents the numerical modeling based on the average state space and controllers design for the four port DC-DC converter. Different operation stages are drawn and simulation for the controllers are shown to lay a solid foundation for developing the experiment.

In chapter 4, a method of maximum power point tracking is developed to explain the operational optimization of wind and solar energy. The simulation results are discussed to verify the proposed topology, following the MPPT control strategy.

Chapter 5 describes the prototype used in the experiment setup and the experimental results, which validate the objectives mentioned in chapter 1. Finally, this dissertation ends with conclusions, a summary of contributions, and recommendations for future work in Chapter 6.

Chapter 2 : A Bidirectional Four-Port DC-DC Converter

2.1 Curit and Topology

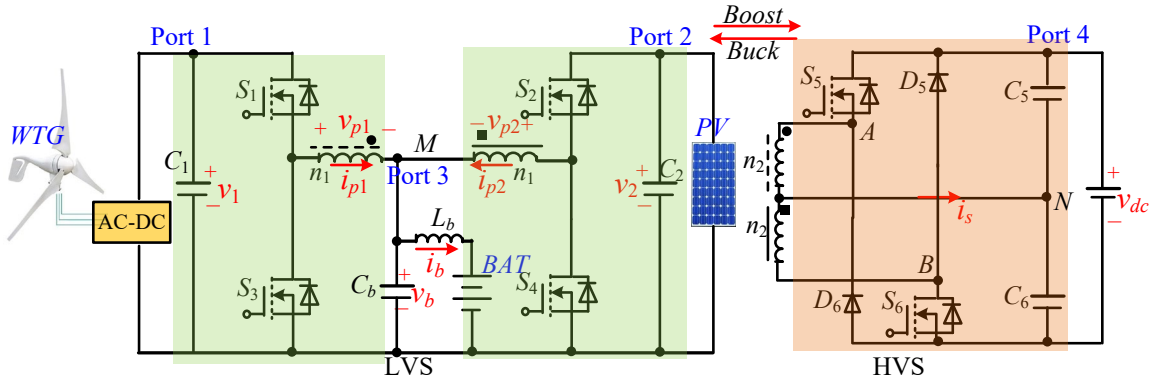

Fig. 2.1 Topology of the proposed four-port DC-DC converter.

Fig. 2.1 shows the topology of the proposed four-port DC-DC converter, which is connected to three different sources: Port 1, Port 2, and Port3 are connected to a WTG, a PV panel, and a battery bank, respectively. Main components of the converters are: S_1, S_2, S_3, S_4, S_5 and S_6 switches, D_5 and D_6 power diodes, and two transformers in series, the capacitors C_1 and C_2 connected to the Port1 and Port2 in parallel respectively, the LC circuit of battery C_b, L_b and two identical capacitors (C_5 and C_6) connected in series which are the output filters.

The transformer whose turns ratio is defined as $n = n_2/n_1$ is modeled as a magnetic inductor L_m in parallel with an ideal transformer and in series with a leak inductor L_s as shown in Fig. 2.2. Since L_m is very large, its current can be neglected. The primary current i_p is then determined by v_p and v_T. The battery is modeled as an ideal battery in series with an internal resistor r_b as shown in Fig. 2.3. V_0 is the ideal voltage source that represents the "open circuit" voltage of the battery, v_b is the battery terminal voltage.

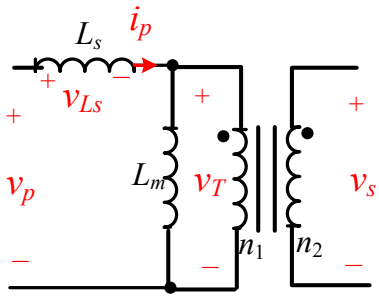

Fig. 2.2 Equivalent circuit of the transformer.

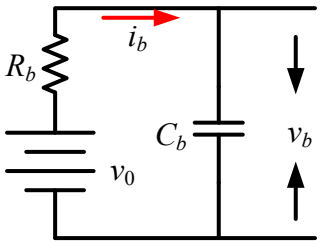

Fig. 2.3 Equivalent circuit of the battery.

2.2 Operating principles

The charging and discharging state switching for the battery of the bidirectional dc/dc converter is the basic architecture of the four-port renewable energy power system. Dynamic behavior characteristics are the same as those in classical buck and boost converters. There are two operating modes of the converter according to the power flow direction of the transformer: buck and boost modes. In the boost mode, the loads in the DC link are supplied by the WTG, PV panel, and battery and the power is delivered from the low voltage side (LVS) to the high voltage side (HVS); in the buck mode, the power flow direction is reversed. For example, when there is surplus power in the microgrid, the battery will be charged to absorb the surplus power.

The proposed converter has six operating scenarios with different states of the switches and values of the duty cycle (d). The duty cycle of the S_5 and S_6 is 0.5, and the PWM of these two switches is complementary. The complementary duty cycle of S_1 and S_2 can be changed from 0 to 1, which is complementary to S_3 and S_4, respectively. The phase shift of the commutation duty cycle of S_1 and S_5 is define as absolute δ. In order to express the state of charge and discharge of battery clearly, the phase shift between the rising edge of v_{gs5} and the falling edge of v_{gs1} in the same period is defined as $\Delta\delta$. Meanwhile,

using the falling edge of v_{gs1} as the benchmark in one cycle, $\Delta\delta$ is negative when the rising edge of v_{gs5} is in the left of the benchmark, which means the battery is charged by the DC link, and positive when the rising edge of v_{gs5} is in the right of the benchmark, which means the battery is discharged to supply power to DC link, and $\Delta\delta = \delta - 1/2$.

Because of the similarity of analysis methods in different operation scenarios, only one operation stage is analyzed in this paper, i.e., $d_1 > 0.5$, $d_2 < 0.5$, and $0.5 < \delta < d_1$, where d_1 and d_2 are duty cycles of S_1 and S_2 respectively. The waveforms in different states of the switches can be drawn as Fig. 2.4. There are four different operation stages in each scenario is shown in Fig. 2.5.

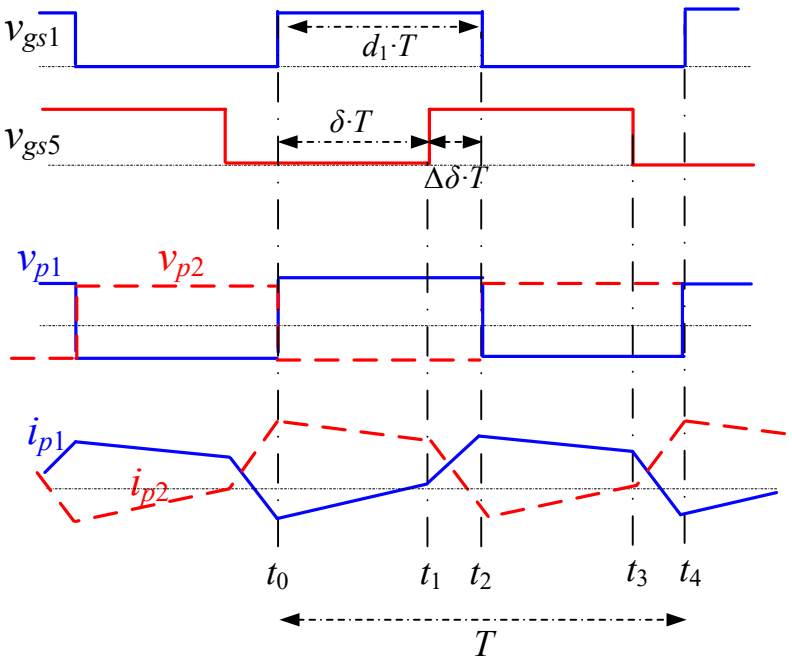

Fig. 2.4 Steady state waveform for converter.

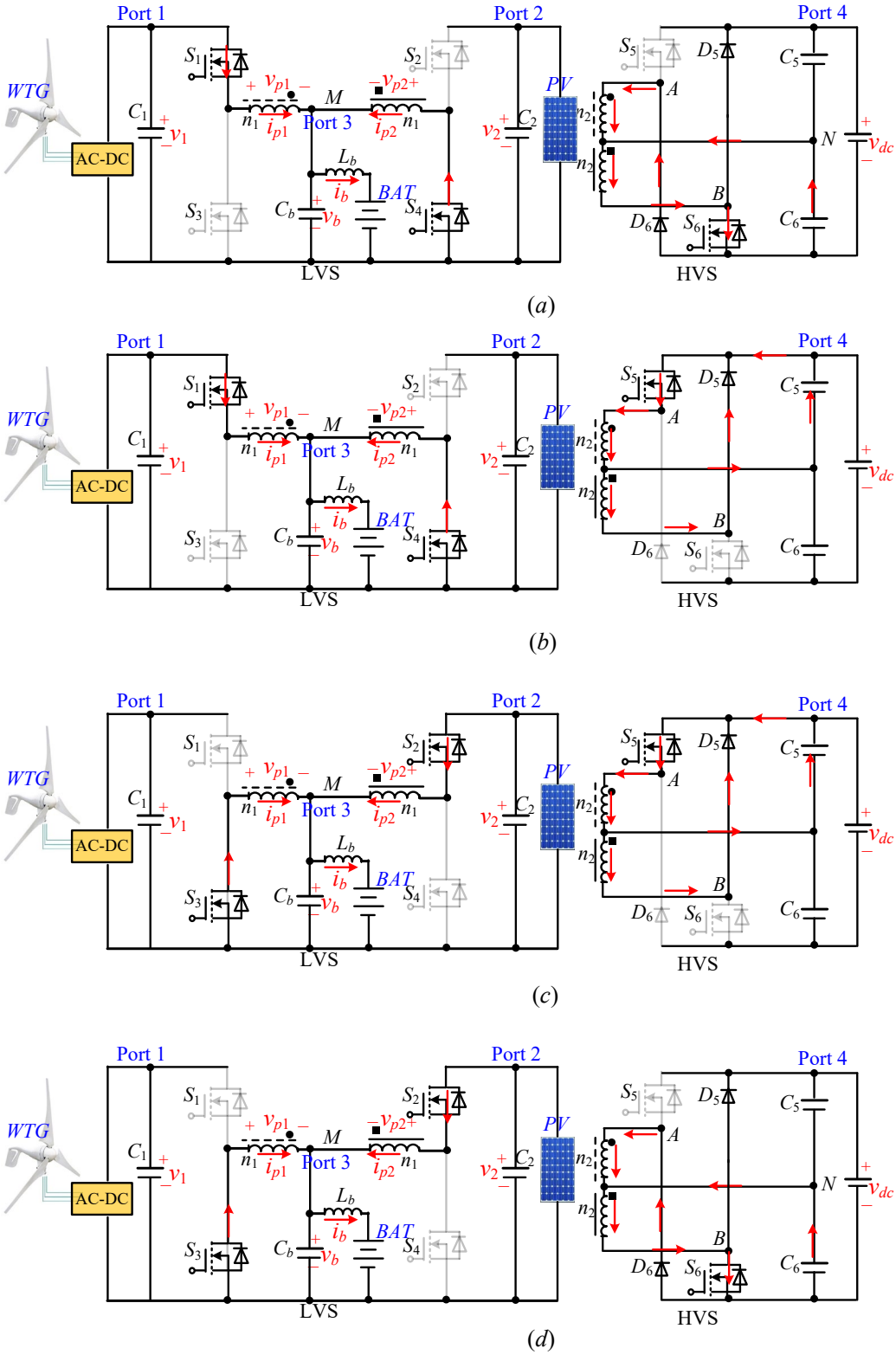

Fig. 2.5 Equivalent circuit of the different operation stages. (*a*) Stage 1. (*b*) Stage 2. (*c*) Stage 3. (*d*) Stage 4.

Stage 1: $t \in [t_0, t_1]$ (see Fig. 2.4), during which S_1 and S_4 are ON, S_5 is off, Port 1 supplies power to the battery and load. The equivalent circuit is shown in Fig. 2.4(*a*), thus $v_{p1} = v_1 - v_b$, on the HVS, the conduction of D_6 clamps $v_{AN} = -v_{dc}/2$, then the voltage across leakages inductors $v_{Ls} = v_1 - v_b - v_{dc}/(2n)$. The differential equation in this stage can be expressed as follows:

$$\frac{di_{p1}}{dt} = \frac{v_1 - v_b - \frac{v_{dc}}{2n}}{L_s} \tag{2.1}$$

where L_s is the leakage inductance on the primary side of the transformers.

Stage 2: $t \in [t_1, t_2]$ (see Fig. 2.4), during which S_1 and S_5 are both on. D_5 is conducted as shown in Fig. 2.4 (*b*), and C_5 is discharged, the power is delivered from the HVS to the LVS, $v_{p1} = v_1 - v_b$. The differential equation in this stage can be expressed as follows:

$$\frac{di_{p1}}{dt} = \frac{v_1 - v_b + \frac{v_{dc}}{2n}}{L_s} \tag{2.2}$$

At the end of this stage, switch S_1 is turned off, i_{p1} decreases and achieves the minimum value at t_1.

Stage 3: $t \in [t_2, t_3]$ (see Fig. 2.4), S_1 is off, S_2 and S_5 are on, as shown in Fig. 2.4 (*c*), the voltage across two primary side of transformer are $-v_b$ and $v_2 - v_b$, respectively. The conduction state of D_6 clamps $v_{AN} = v_{dc}/2$, then $v_{Ls} = -v_b + v_{dc}/(2n)$. The differential equation is this stage can be expressed as bellow:

$$\frac{di_{p1}}{dt} = \frac{-v_b + \frac{v_{dc}}{2n}}{L_s} \tag{2.3}$$

Stage 3: $t \in [t_3, t_4]$ (see Fig. 2.4), during which S_1 and S_5 are both off, as shown in Fig. 2.4 (*d*), the voltage across two primary sides of transformers are $-v_b$ and $v_2 - v_b$, respectively. The conduction state of D_6 clamps $v_{AN} = -v_{dc}/2$, then $v_{Ls} = -v_b - v_{dc}/(2n)$. The differential equation in this state can be presented as follows:

$$\frac{di_{p1}}{dt} = \frac{-v_b - \frac{v_{dc}}{2n}}{L_s} \tag{2.4}$$

According to the steady state waveform and the differential equations for the four stages, the i_{p1} can be deduced by integration of the current i_{p1} waveform. Assuming the initial steady-state current of i_p1 is I_0, i.e., $i_{p1}(0) = I_0$, then the current in the four stages can be calculated as follows:

$$i_{p1}(t) = \begin{cases} I_0 + \frac{1}{L_s}\left(v_1 - v_b + \frac{v_{dc}}{2n}\right)\cdot t & t_0 \le t \le t_1 \\ i_{p1}(t_1) + \frac{1}{L_s}\left(v_1 - v_b - \frac{v_{dc}}{2n}\right)\cdot t & t_1 \le t \le t_2 \\ i_{p1}(t_2) + \frac{1}{L_s}\left(-v_b + \frac{v_{dc}}{2n}\right)\cdot t & t_2 \le t \le t_3 \\ i_{p1}(t_3) + \frac{1}{L_s}\left(-v_b - \frac{v_{dc}}{2n}\right)\cdot t & t_3 \le t \le t_4 \end{cases} \tag{2.5}$$

The power through one transformer can be calculated by $P = V_T \times i_{p1}$, where $V_T = v_{dc}/2n$, i_{p1} is the mean value calculated according to the waveform shown in Fig. 2.4. The expression of the power can be deduced as follows:

$$p_1 = \frac{v_{dc}}{2n}\left[\frac{2}{T}\left[\int_{t_0}^{t_1} i_{p1}(t)\,dt + \int_{t_{43}}^{t_4} i_{p1}(t)\,dt\right] - \frac{2}{T}\int_{t_1}^{t_3} i_{p1}(t)\,dt\right]$$
$$= \underbrace{\frac{v_{dc}\cdot v_1}{2n\cdot L_s\cdot f_s}}_{K}\left(-d_1^{\,2} + 2\delta\cdot d_1 - 2\delta + \frac{1}{2}d_1 + \frac{1}{2}\right) \tag{2.6}$$

Due to the symmetric structure of converter, the power transferred through the other transformer can be derived using the same method and the total power delivered between the LVS and HVS is

$$p = K\cdot\left[-4\delta + 1 - \left(d_1^{\,2} + d_2^{\,2}\right) + \left(2\delta + \frac{1}{2}\right)\cdot\left(d_1 + d_2\right)\right] \tag{2.7}$$

Similarly, the amount of power in other scenarios can be derived as well, e.g., when $0 < \delta < 0.5$ or $d_1 < \delta < 1$. The expression of power in different scenarios has been shown as follows:

$$p = \begin{cases} k\cdot\left[-4\delta^2 - \left(d_1^{\,2} + d_2^{\,2}\right) + \left(2\delta + \frac{1}{2}\right)\cdot\left(d_1 + d_2\right)\right] & 0<\delta \le 0.5 \\ k\cdot\left[-4\delta + 1 - \left(d_1^{\,2} + d_2^{\,2}\right) + \left(2\delta + \frac{1}{2}\right)\cdot\left(d_1 + d_2\right)\right] & 0.5<\delta < d_1 \\ k\cdot\left[4\delta^2 - 4\delta + 1 + \left(d_1^{\,2} + d_2^{\,2}\right) + \left(\frac{1}{2} - 2\delta\right)\cdot\left(d_1 + d_2\right)\right] & \mathrm{d}_1 \le \delta < 1 \end{cases} \tag{2.8}$$

Particularly, when $d_1 = d_2 = 0.5$, the expression of power flow can be simplified as:

$$p = \begin{cases} k\cdot\left(-4\delta^2 + 2\delta\right) & 0 < \delta < 0.5 \\ k\cdot\left(4\delta^2 - 6\delta + 2\right) & 0.5 \le \delta < 1 \end{cases} \tag{2.9}$$

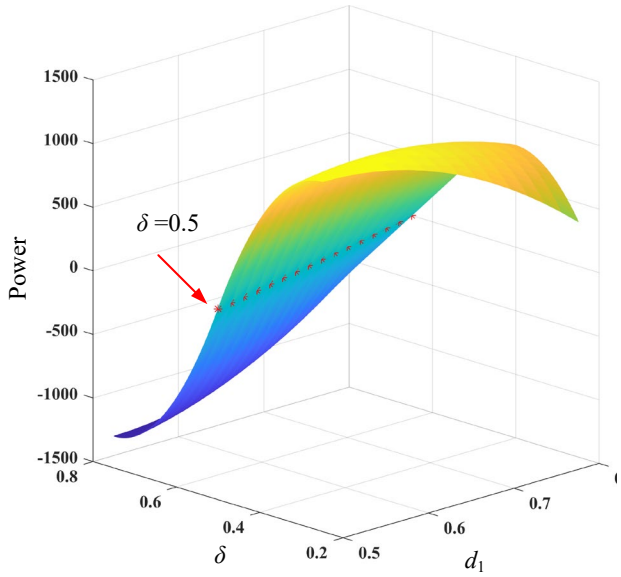

Fig. 2.6 The 3*D* view of power.

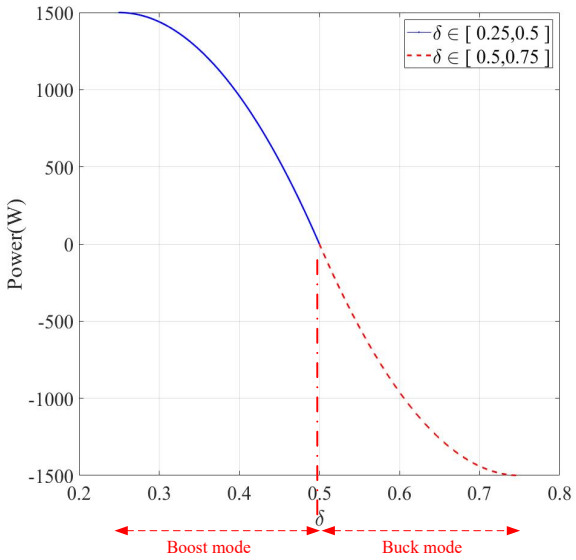

Fig. 2.7 The 2*D* view of power when d_1=0.5.

The 3*D* view of the power at $d_1 = d_2 = 0.5$ is illustrated in Fig. 2.6. As shown in Fig. 2.6, for a fixed $\delta = 0.5$, the maximum power increases with d_1. The curve of the power vs δ at $d_1 = d_2 = 0.5$ is illustrated in Fig. 2.7. As shown in Fig. 2.7, when $\delta < 0.5$, battery is charged, the amount of charge power is decreased with the increase of δ, i.e., $p = 0$ when $\delta = 0.5$ and p has a maximum value when $\delta = 0.25$; similarly, battery is discharged when $\delta > 0.5$, the maximum discharge power is achieved when $\delta = 0.75$. Therefore, the charge/discharge state can be controlled by regulating δ within the range of [0.25, 0.75].

2.3 ZVS analysis

2.3.1 Design consideration

Zero-voltage switching (ZVS), also known as soft switching, is always be used for high frequency and higher efficiency requirements, which allows switches to operate at a high frequency and at high input voltages without sacrificing efficiency. This technique, like virtually all contemporary switching voltage regulators, uses PWM-based operation,

but with an additional separate phase to the PWM timing to allow for ZVS operation, which enables the voltage regulator to avoid the switching losses that are typically incurred during hard switching.

Hard switching occurs during the overlap between voltage and current when switching on the MOSFET as shown in Fig. 2.8. The voltage v_{DS} decreases while current exist after the MOSFET is turned on, which lead to the overlap between voltage and current and producing losses. This deficiency can be further improved by ZVS, as shown in Fig. 2.8 (b). During the switching on period, voltage falls to zero before the MOSFET is turned on, during the overall transient, current (i_{DS}) is zero, which indicate there is no overlap between voltage v_{DS} and current i_{DS} thus the turning-on loss is zero.

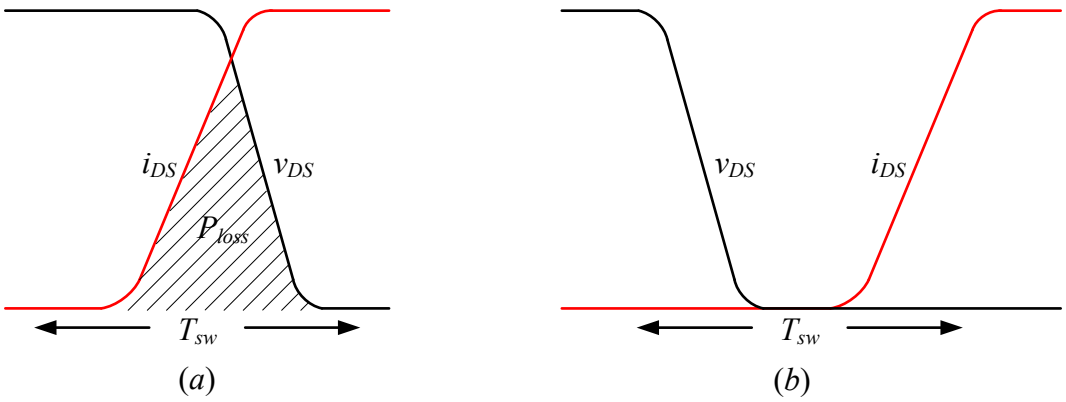

Fig. 2.8 (*a*) Hard switched turn on (*b*) soft switch turn on.

When a MOSFET turns on, there are losses due to the discharge of stored energy in its C_{oss} capacitor leading to the overlap (shown as Fig. 2.9 (*a*)). In ZVS the *Coss* is tricked into discharging its energy prior to turning on the MOSFET. Usually the MOSFET's body diode goes into conduction in the process.

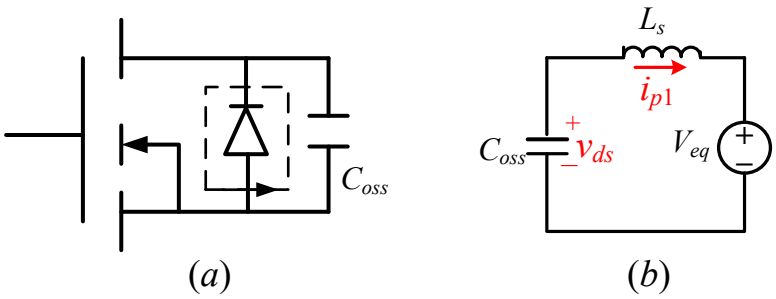

Fig. 2.9 (*a*) The feature of the MOSFET (*b*) the equivalent circuit of S_2

2.3.2 ZVS analysis

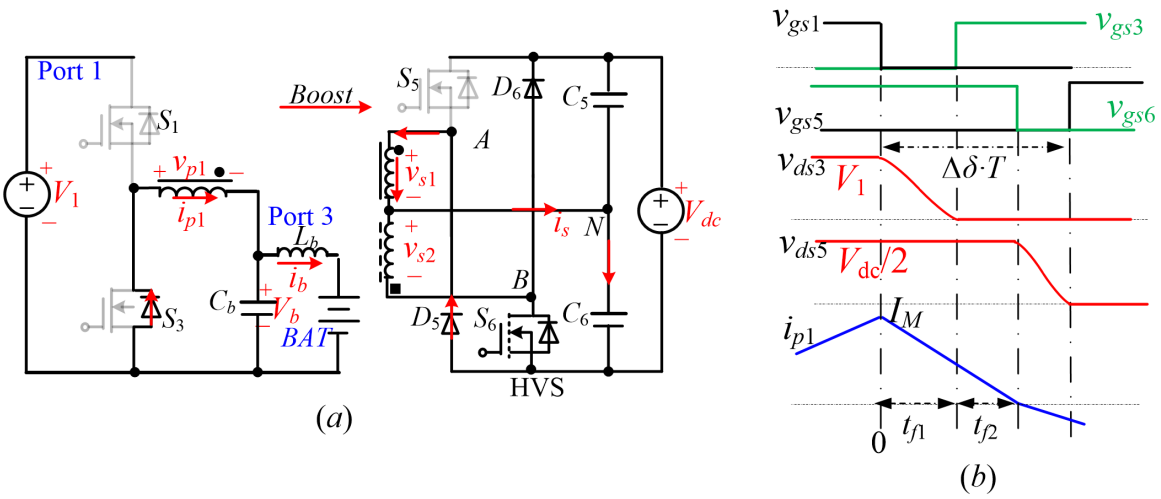

Fig. 2.10 (*a*) The instant of S_1 turning off (*b*) the waveforms of the instant.

Take case of the boost mode, the waveform of the circuit at the moment of S_1 turning off is shown in Fig. 2.10. The initial values of v_{p1}, v_{s1}, V_T are as follows in an instant: $v_{p1} = v_{ds} - V_b$, $v_{s1} = -V_{dc}/2$, $V_T = V_{dc}/(2n)$. The differential equation of the transformer can be deduced as follows:

$$L_s \frac{di_{p1}}{dt} = v_{ds} - V_b - V_T = v_{ds} - \underbrace{\left(V_b + \frac{V_{dc}}{2n}\right)}_{V_{eq}} \tag{2.10}$$

The equivalent circuit can be modelled as Fig. 2.9 (*b*). Then

$$\begin{cases} L_s \dfrac{di_{p1}}{dt} = v_{ds} - V_{eq} \\ C_{oss} \dfrac{dv_{ds}}{dt} = -i_{p1} \end{cases} \tag{2.11}$$

Then $$L_s \cdot C_{oss} \cdot \frac{dv_{ds}^2}{dt^2} + v_{ds} = V_{eq} \tag{2.12}$$

v_{ds} (0) = V_1, $i_{p1}(0) = I_M$ in the instant, so

$$\begin{cases} v_{ds} = \left(V_1 - V_{eq}\right) \cdot \cos\left(\omega_r \cdot t\right) - I_M \cdot Z_r \cdot \sin\left(\omega_r \cdot t\right) + V_{eq} \\ i_{p1} = \dfrac{V_1 - V_{eq}}{Z_r} \cdot \sin\left(\omega_r \cdot t\right) + I_M \cdot \cos\left(\omega_r \cdot t\right) \end{cases} \tag{2.13}$$

where $\omega_r = \dfrac{1}{\sqrt{L_s \cdot C_{oss}}}$, $Z_r = \dfrac{1}{\omega_r \cdot C_{oss}} = \sqrt{\dfrac{C_{oss}}{L_s}}$.

When $\dfrac{dv_{ds}}{d\left(\omega_r t\right)} = 0$, that is $\tan\left(\omega_r \cdot t\right) = -\dfrac{I_M \cdot Z_r}{V_1 - V_{eq}}$, v_{ds} has the minimum value as follows:

$$v_{ds,\min} = V_{eq} - \sqrt{\left(V_1 - V_{eq}\right)^2 + \left(I_M \cdot Z_r\right)^2} \tag{2.14}$$

To achieve the ZVS condition for S_3, $v_{ds,\min} \le 0$. When the d_1=0.5, $V_1 = 2V_b$. So

$$I_M \ge \frac{\sqrt{2V_{dc} \cdot V_b / n}}{Z_r} \tag{2.15}$$

According to the expression of the $i_{p1}(t)$ shown in (2.5), the current of battery can be deduced:

$$\begin{aligned} I_b &= \frac{2}{T}\int_0^T i_{p1}\left(t\right) \cdot dt = 2I_M - \frac{1}{2f_s L_s} \cdot \left[V_b - \frac{V_{dc}}{2n} \cdot \left(4 \cdot \Delta\delta^2 - 3 \cdot \Delta\delta + 1\right) \right] \\ &= \frac{V_{dc}}{n \cdot L_s \cdot f_s} \cdot \Delta\delta \cdot \left(1 + 2 \cdot \Delta\delta\right) \end{aligned} \tag{2.16}$$

So the expression in (2.15) can be further deduced as follows:

$$I_M = \frac{1}{4 f_s L_s} \cdot \left[V_b - \frac{V_{dc}}{2n} \cdot \left(12 \cdot \Delta\delta^2 + \Delta\delta + 1 \right) \right] \geq \frac{\sqrt{2 V_{dc} \cdot V_b / n}}{Z_r} \tag{2.17}$$

For the ZVS condition of S_5, the time t_{f1} S_3 takes from v_{ds3}=V$_1$ to v_{ds3}=0 is as follows:

$$t_{f1} = \pi \cdot \sqrt{L_s \cdot C_{oss}} \tag{2.18}$$

After v_{ds3}=0, that is to say, S_3 is on, then the differential equation of the transformer is shown as follows:

$$L_s \frac{di_{p1}}{dt} = -V_b - V_T = -V_{eq} \tag{2.19}$$

When $i_{p1} < 0$, i_{s1} changes the direction and drops to zero, after i_{p1} changes the polarity, v_{ds5} decreases, $v_{s1} = V_{dc}/2 - v_{ds5}$, $V_T = -V_{dc}/2 + v_{ds5}$, the expression for the transformer is as follows:

$$\begin{cases} L_s \dfrac{di_{p1}}{dt} = -V_b - \dfrac{-V_{dc}/2 + v_{ds5}}{n} = -\dfrac{v_{ds5}}{n} + \dfrac{V_{dc}}{2n} - V_b \\ n \cdot i_{p1} = C_{oss} \cdot \dfrac{dv_{ds5}}{dt} \end{cases} \tag{2.20}$$

The initial condition is v_{ds} (0) = V_{dc}/2, i_{p1}(0) = C_{oss}· dv_{ds}(0)/dt = 0, so

$$v_{ds5} = nV_b \cdot \cos\left(\omega_{r2} \cdot t \right) + \left(\frac{V_{dc}}{2} - nV_b \right) \tag{2.21}$$

Where $\omega_{r2} = \dfrac{1}{\sqrt{n \cdot L_s \cdot C_{oss}}}$, $Z_{r2} = \omega_{r2} \cdot C_{oss} = \sqrt{\dfrac{n \cdot C_{oss}}{L_s}}$. When v_{ds5} = 0,

$$t_{f2} = \frac{1}{\omega_{r2}} \cdot \cos^{-1}\left(1 - \frac{V_{dc}}{2n \cdot V_b} \right) \tag{2.22}$$

Therefore, the ZVS condition for S_5 is as follows:

$$\frac{t_{f1}+t_{f2}}{T} \le \Delta\delta \tag{2.23}$$

The 3-D view of ZVS of S_3 and S_5 is shown in Fig. 2.11(a), ZVS is decided by v_{dc}, δ and power. The 2-D view of ZVS of S_3 and S_5 is shown in Fig. 2.11(b). It can be seen that S_1 and S_3 can achieve ZVS all the time, S_5 can achieve ZVS when δ >0.538 or $\Delta\delta$ > 0.038.

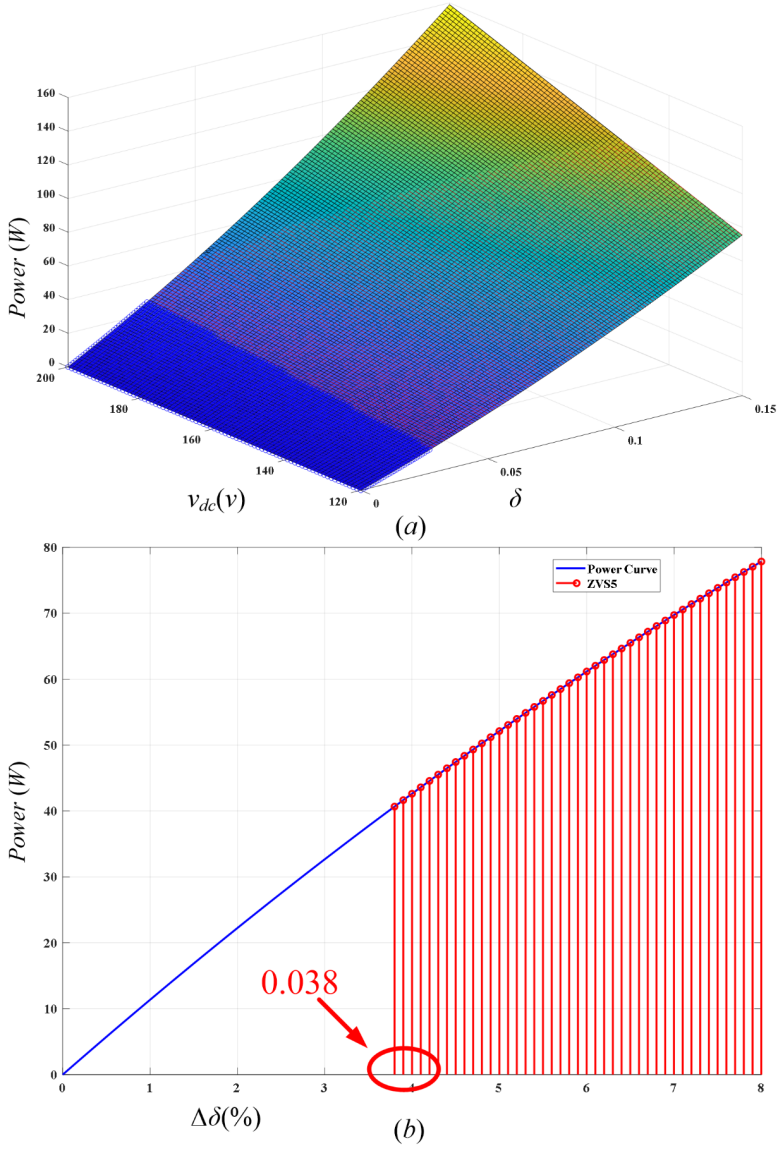

Fig. 2.11 (a) The ZVS 3-D view of S_3 and S_5 (b) The ZVS 2-D view of S_3 and S_5.

2.3.3 Experiment results

To verify the theory of the ZVS analysis, the waveforms are measured when the converter works in the boost mode. Fig. 2.12 shows the ZVS of S_1 and S_3, where the phase shift δ between v_{gs1} and v_{gs5} is 0.65. The experiment testified that the switches S_1 and S_3 can achieve ZVS at any value of δ, which is consistent with the calculation. Fig. 2.13 shows the hard switching of switch S_5, where the phase shift δ between v_{gs1} and v_{gs5} is 0.525. Fig. 2.14 shows the critical condition of ZVS of switch S_5, where δ is 0.533. Fig. 2.15 shows the ZVS of switch S_5, where δ is 0.535, which proves that S_5 can achieve ZVS when δ>0.533. The theoretically critical ZVS condition of S_5 is δ=0.538, which is in agreement with the experiments in the range of the allowable error. In addition, as shown in pictures, before the gate signals $v_{gs1,}$ v_{gs3} and v_{gs5} are applied, $v_{ds1,}$ v_{ds3} and v_{ds4} have already dropped to zero, which indicates $S_{1,}$ S_3 and S_5 are turned ON under the ZVS condition. Thus the ZVS theoretical calculation is verified by the experiments.

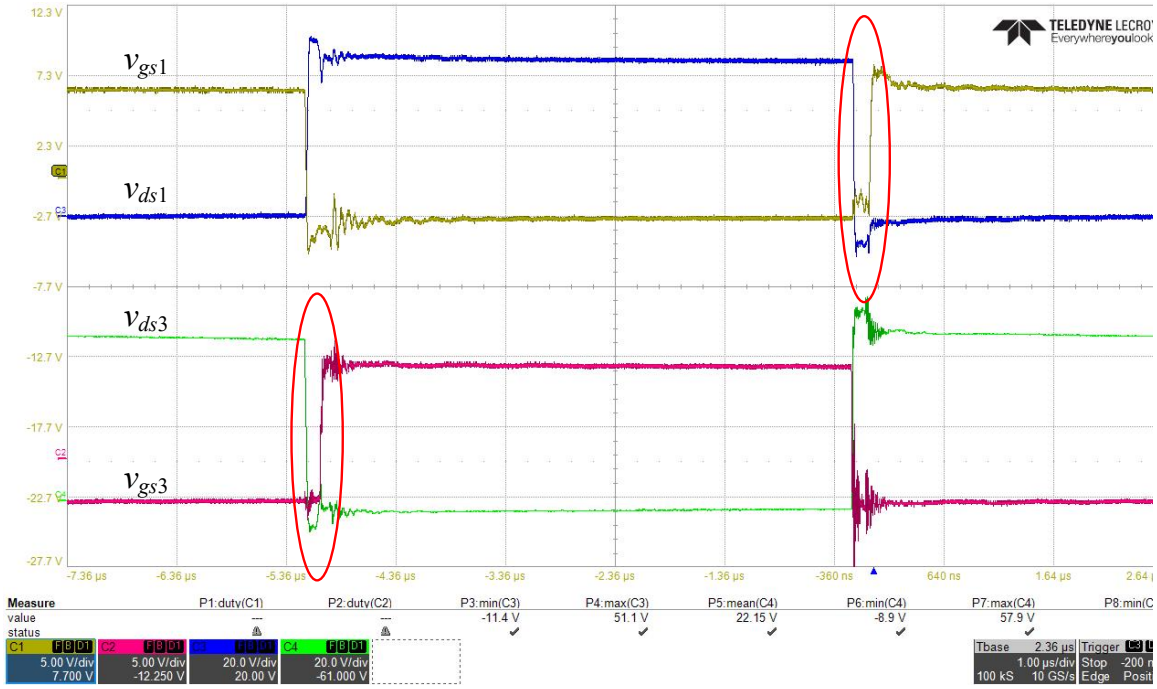

Fig. 2.12 ZVS of S_1 and S_3.

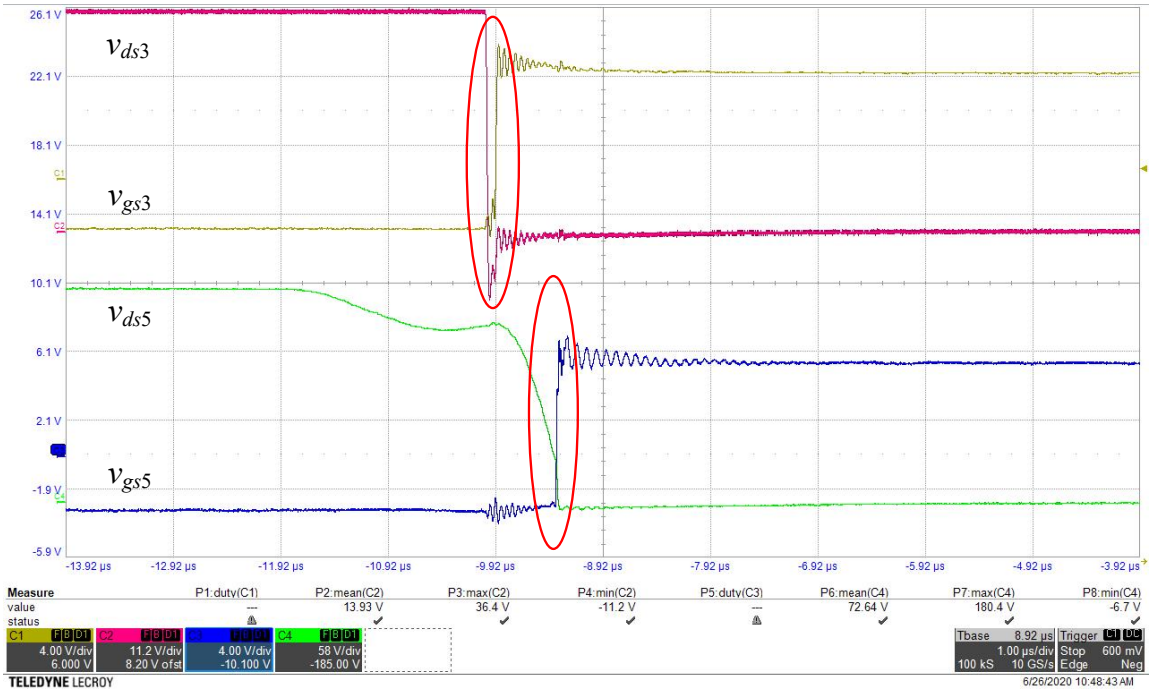

Fig. 2.13 Hard switch of S_5 when $\Delta\delta = 0.025$.

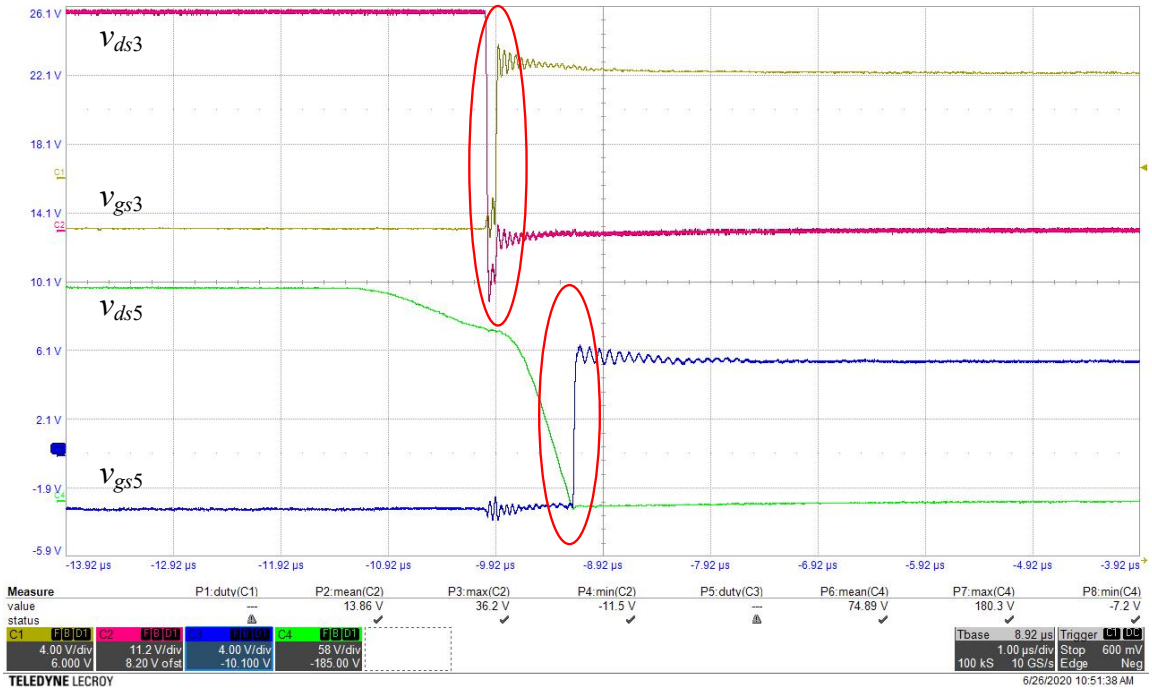

Fig. 2.14 critical ZVS of S_5 when $\Delta\delta = 0.033$.

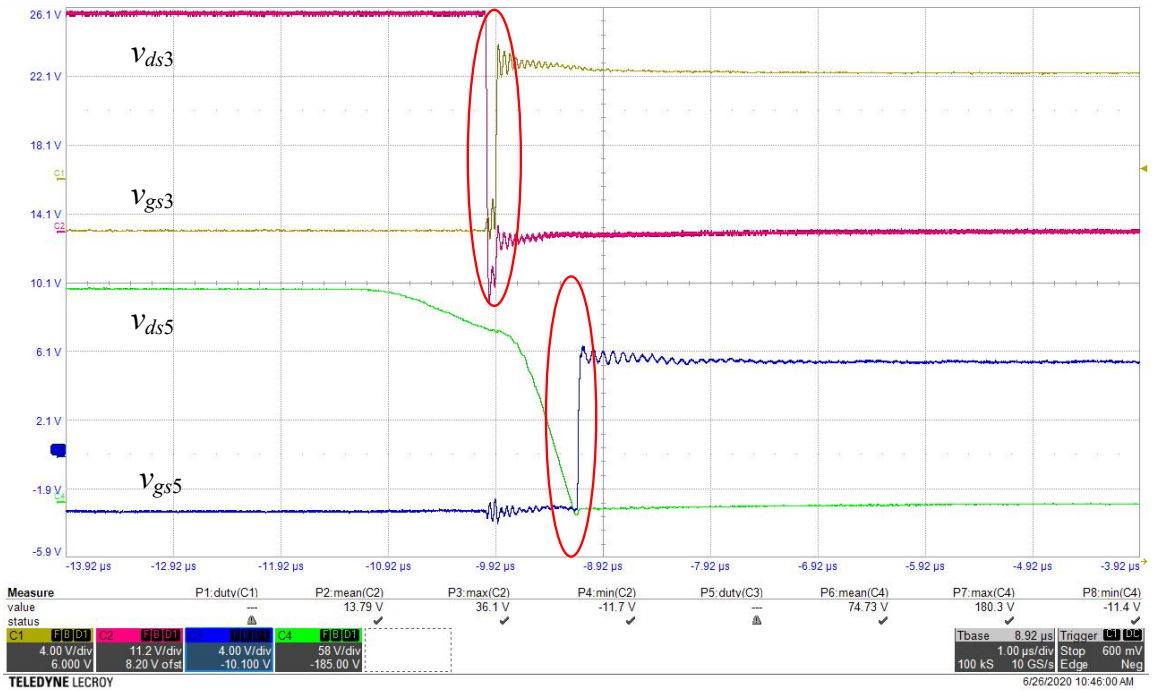

Fig. 2.15 ZVS of S_5 when $\Delta\delta = 0.035$.

Chapter 3 : Modeling and Controller Design for Proposed Converter

3.1 Modeling and Controller Design for the Four-port DC-DC Converter

As mentioned previously in chapter 2, when the battery works in the charge mode, the power depicted in (6) can be considered as the power flowing through the battery. The equivalent circuit on the battery side is shown in Fig. 3.1, where $i_{tb} = P/V_b$; r_b and V_{boc} are the internal resistance and open circuit voltage of the battery, respectively. According to the Kirchhoffs Circuit Law (KVL and KCL), the differential equations of the battery is as follows:

$$\begin{cases} v_b = L_b \dfrac{di_b}{dt} + i_b r_b + V_{boc} \\ i_{tb} = C_b \dfrac{dv_b}{dt} + i_b \end{cases} \tag{3.1}$$

With the Laplace transform, (3.1) can be written as:

$$\begin{cases} v_b(s) = L_b s \cdot i_b(s) + r_b i_b(s) + V_{boc} \\ i_{tb}(s) = C_b s \cdot v_b(s) + i_b(s) \end{cases} \tag{3.2}$$

After introducing the small signal in the model, the variation of V_{boc} can be taken as zero thus

$$G_{v_b\_i_b}(s) = \frac{v_b(s)}{i_b(s)} = L_b \cdot s + r_b \tag{3.3}$$

$$\frac{i_b(s)}{i_{tb}(s)} = \frac{1}{C_b L_b s^2 + C_b r_b s + 1} \tag{3.4}$$

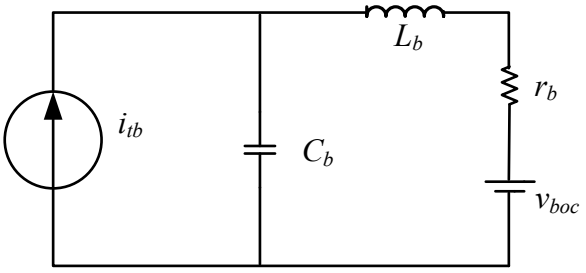

Fig. 3.1 Equivalent circuit on the battery side.

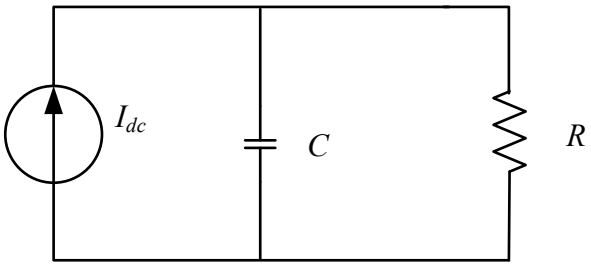

Fig. 3.2 Equivalent circuit on the load side.

Assuming d_1=0.5 to simplify the expression of the $i_{tb} = P/V_b$, then

$$i_{tb}(s) = k \cdot \frac{1}{v_b} \cdot \left(-\delta(s) + \frac{1}{2} \right) \tag{3.5}$$

The value 1/2 can be neglected, thus the transfer function of $i_{tb\_\delta}(s)$ can be derived as bellow:

$$\frac{i_{tb}(s)}{\delta(s)} = -\frac{k}{v_b} \tag{3.6}$$

According to (3.4) and (3.6), the transfer function of $Gi_{b\_\delta}(s)$ can be deduced as follows:

$$G_{ib\_\delta}(s) = \frac{i_b(s)}{\delta(s)} = \frac{i_b(s)}{i_{tb}(s)} \cdot \frac{i_{tb}(s)}{\delta(s)} = -\frac{k}{v_b} \cdot \frac{1}{C_b L_b s^2 + C_b r_b s + 1} \tag{3.7}$$

Similarly, when the converter works in the discharge mode, $I_{dc} = P/V_{dc}$. The equivalent circuit on the DC link side can be modelled as shown in Fig. 3.2, where R is the load. The differential equation is shown as follows:

$$i_{dc} = C \frac{dv_{dc}}{dt} + \frac{v_{dc}}{R} \tag{3.8}$$

Using the Laplace Transform,

$$i_{dc}(s) = \left(C \cdot s + \frac{1}{R} \right) v_{dc}(s) \tag{3.9}$$

Assuming $d_1 = 0.5$ to simplify the expression of the $I_{dc} = P/V_{dc}$, then

$$i_{dc}(s) = \frac{v_1}{2n \cdot f \cdot L_s}(-\delta(s) + \frac{1}{2}) \tag{3.10}$$

According to (3.9) and (3.10), the transfer functions G_{vdc_δ} (s) can be derived by ignoring the constant value 1/2. Combining (3.7) and (3.10), the transfer function of G_{vdc_ib} (s) can be derived:

$$G_{vdc\_\delta} = G_{vdc\_idc} \cdot G_{idc\_\delta} = \frac{1}{Cs + 1/R} \cdot \frac{-v_1}{2 \cdot n \cdot L_s \cdot f} \tag{3.11}$$

$$G_{vdc\_ib}(s) = \frac{G_{vdc\_\delta}(s)}{G_{ib\_\delta}(s)} = \frac{v_b \cdot (C_b L_b s^2 + C_b r_b s + 1)}{v_{dc} \cdot (C_{dc} s + 1/R)} \tag{3.12}$$

As indicated in (3.3) and (3.12), the battery voltage v_b and the DC link voltage v_{dc} can both be controlled by i_b. Fig. 3.3 show the signal flows of the overall system and organization of four controllers: G_{cvb}(s) and G_{cib}(s) are used for controlling v_b and i_b, respectively; G_{cvdc}(s) is used to control v_{dc}. While $G_{\delta d}$(s) is designed for eliminating the influence of d toward i_b. The decoupling controller $G_{\delta d}$(s) can be derived as follows:

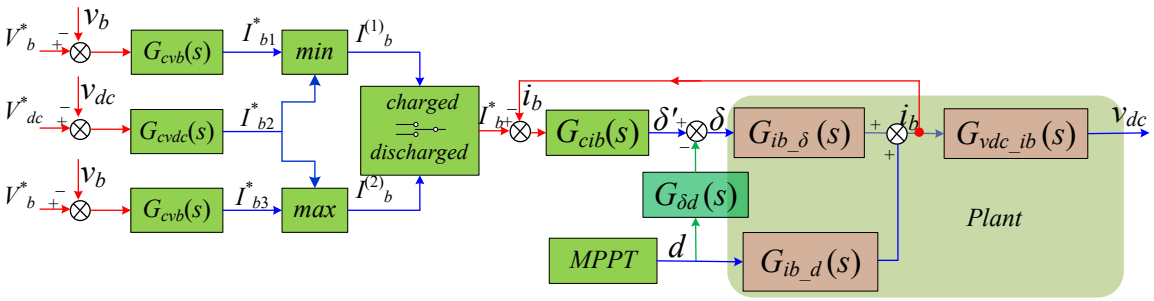

Fig. 3.3 Topology of the proposed four-port DC-DC converter.

$$G_{\delta d}(s)=\frac{G_{ib\_d}(s)}{G_{ib\_\delta}(s)}=\frac{1}{2} \tag{3.13}$$

With the decoupling controller, the controllers G_{cib}(s) and G_{cvb}(s) then can be designed with the transfer functions G_{ib_δ}(s) and G_{vb_ib}(s) independently.

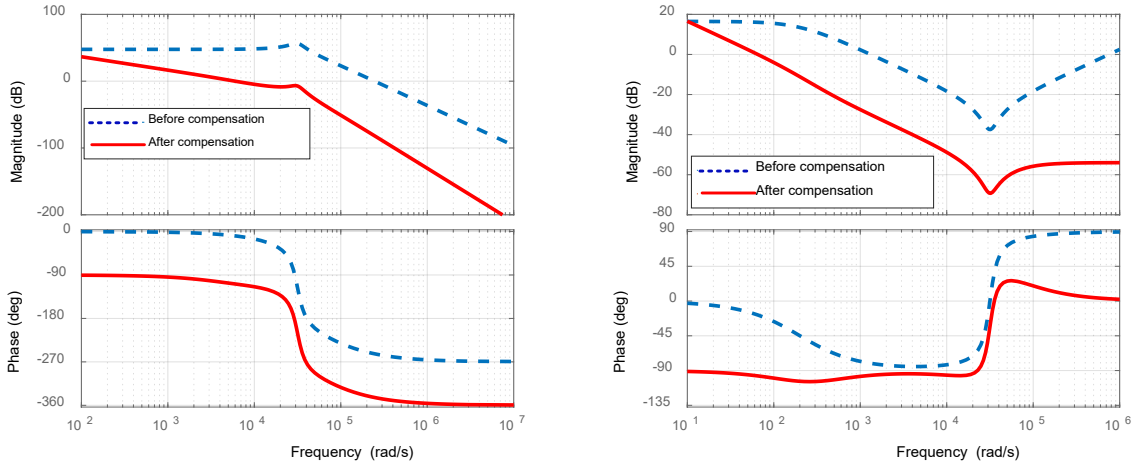

Fig. 3.4 Bode plot: (*a*) G_{ib_δ}(s) without and with G_{cib}(s); (*b*) G_{vdc_ib}(s) before and after using G_{cvdc}(s).

Fig. 3.4 shows the bode plots with and without G_{cib}(s) and G_{cvdc}(s). The parameters of the PI controller which has the following forms shown as (3.14) are summarized in TABLE I.

$$G(s)=\frac{k_p\cdot(s+k_i)}{s\cdot(s+p)} \tag{3.14}$$

TABLE *I*: Parameters of the controllers.

PI controller	$G_{cvb}(s)$	$G_{cib}(s)$	$G_{cvdc}(s)$
Portion (k_p)	1800	20	1500
Integral (k_i)	700	8000	330
Pole (p)	440	5700	4.9×10^4

3.2 Experiment results

In order to verify these controllers, experiments are developed following by simulations. Fig. 3.5 shows the measured responses of the battery current controller. When the battery is controlled from charge mode to discharge mode, the battery current (i_b) decreases from original reference 2 A to new reference value – 2 A and δ increases from 0.47 to 0.59, which testify the stability and reliability of the controller G_{cib}(s). Fig. 3.6 shows the measured dynamic responses of the DC-link voltage (v_{dc}). As shown in Fig. 3.6, at first the converter is working on the grid connected mode. When the DC microgrid is removed, δ is increased from 0.43 to 0.49 and the battery quickly switches from the charge mode to the discharge mode. During the transient, v_{dc} first drops and then increases to its reference value within 300 *ms*, which validates the effectiveness of G_{cib}(s) and G_{cvdc}(s). At the same time, the experiment results manifest again that the converter can work in buck and boost mode and the controller of i_b works well.

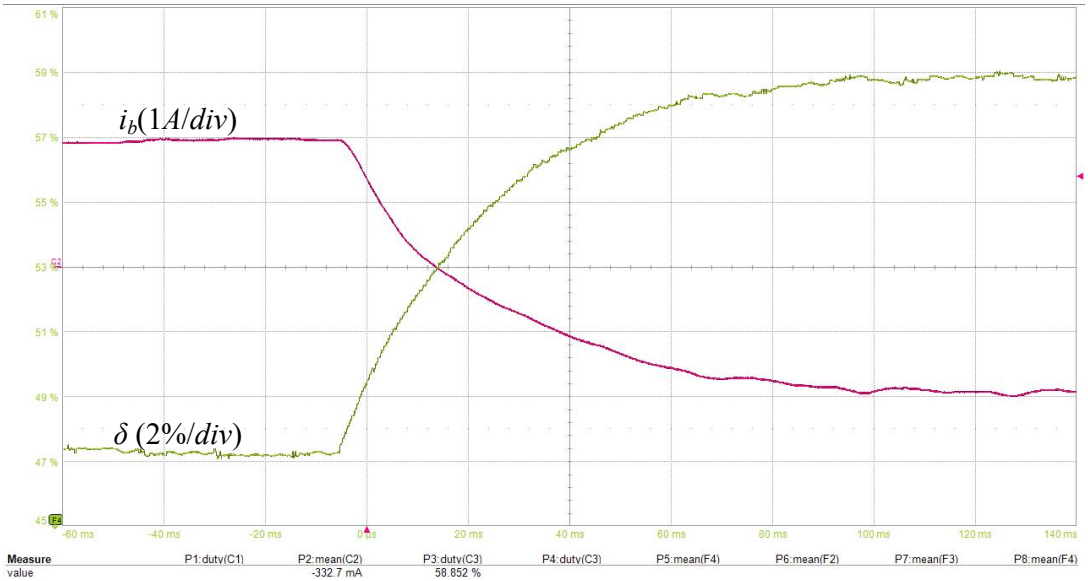

Fig. 3.5 The dynamic response of i_b when its reference value is changed from 2A to – 2A.

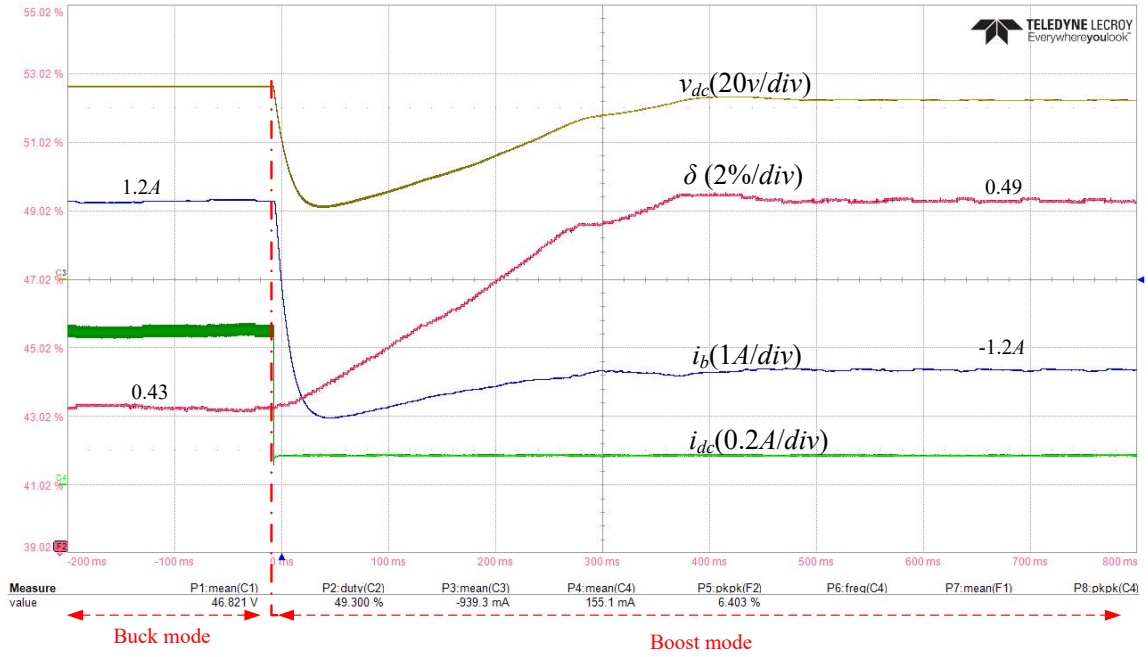

Fig. 3.6 The dynamic response of v_{dc} controller.

3.3 Power management

All controllers regulate both the DC link voltage and the battery charging/discharging. The phase shift δ serves as the key control variable to achieve the power balance and automatic control in different operation scenarios of the whole power generation system. There are three control loops by taking charge of δ, i_b and the duty cycle d_1, d_2, namely the DC link voltage loop, battery current and voltage loop. The priority controller determines which control loop is enable. The objective is to achieve the power balance of the whole power system and automatic battery charging/discharging management, while maintaining the maximum power point tracking (MPPT) for the RES. As mentioned before, microgrid can work in either stand-alone mode or grid-connected mode. The different power flows in these two mode are shown in Fig. 3.7.

1) Stand-alone mode

When the converter works in the stand-alone mode, the converter operates as the boost mode. When the load power is larger than the PV and wind turbine maximum output power, but within the most power that the PV, wind turbine and battery can supply in combination, the DC link voltage control loop and battery voltage loop would be enabled to utilize the maximum I^*_b. Meanwhile, the battery would operate in the discharging mode and supply a part of the load power shown as Fig.3.7 (*a*). When the load power is larger than the most power that the three ports can supply in combination, the DC link voltage control loop and battery voltage loop would be enabled to utilize the minimum I^*_b. And the battery would operate in the charging mode to absorb the excess power shown as Fig.3.7 (*b*).

2) Grid-connected mode

When the converter works in the grid-connected mode, the converter operates as the buck mode. The surplus power in the grid will be stored to the battery, i.e., the power flow is reversed compared to the boost mode as shown in Fig.3.7 (c).

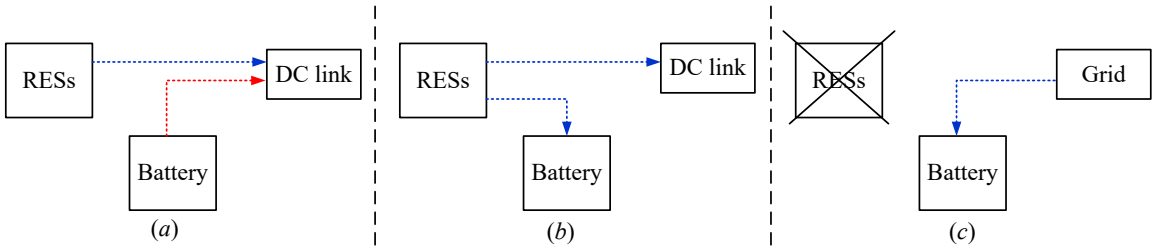

Fig. 3.7 Power management scenarios: (*a*) load power > P_{RESs}; (*b*) load power < P_{RESs}; (*C*) grid-connected mode.

Chapter 4 : Maximum Power Point Tracking for Multiple Different RESs

Maximum power point tracking (MPPT) is an algorithm which has been widely applied in wind turbines and photovoltaic (PV) solar systems to maximize power extraction under all conditions, thus ultimately providing the high-operational efficiencies at creating wind or solar energy. The primary principle of MPPT is to extract the maximum available power from energy generators by making them operate at the most efficient voltage, where it is also known as maximum power point (MPP).

4.1 Control Strategy for Maximum Power Point Tracking of PV System

PV system, which is a bunch of individual PV cells connected in series and parallel to construct a PV array, can directly convert the incident solar radiation into electric energy. The output power of a PV system changes depending on solar radiation (S), as well as other factors such as temperature (T), and the age of the cell, which varies randomly, so how to control the PV system always works on the maximum output power has become increasing important both strategically and economically. In order to always get the maximum extracted power from PV system, the technique MPPT is employed.

According to PV's characteristics, PV system has a single operating point where the values of the current (I) and voltage (V) of the cell result in a maximum power output in any given set of operational conditions. The power P can be calculated by $P=V\cdot I$. The power-voltage curve and current-voltage curve are presented on Fig. 4.1. From the picture, the power delivered from or to a device is optimized where the derivative (graphically, the

slope) $dP/dV = 0$. This is known as the MPP and corresponds to the "knee" of the curve. By its very nature, the control strategy of MPPT is emerging to control PV always work in the vicinity of t MPP.

Based on the characteristic that the slope $dP/dV=0$ at MPP, the controller of MPPT can be designed to track the incrementing conductance $\Delta P/\Delta V$. There are three regions according the slop of the *P-V* characteristic curve of the PV shown in (4.1).

$$\begin{cases} \dfrac{dP}{dV} = 0 & \text{at MPP} \\ \dfrac{dP}{dV} > 0 & \text{on the left of MPP} \\ \dfrac{dP}{dV} < 0 & \text{on the right of MPP} \end{cases} \tag{4.1}$$

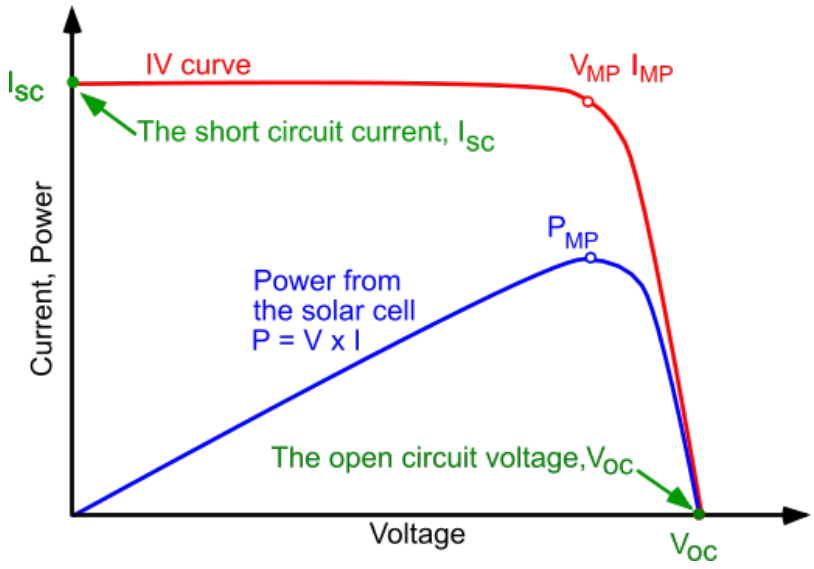

Fig. 4.1 PV *P-V* characteristic and *I-V* characteristic

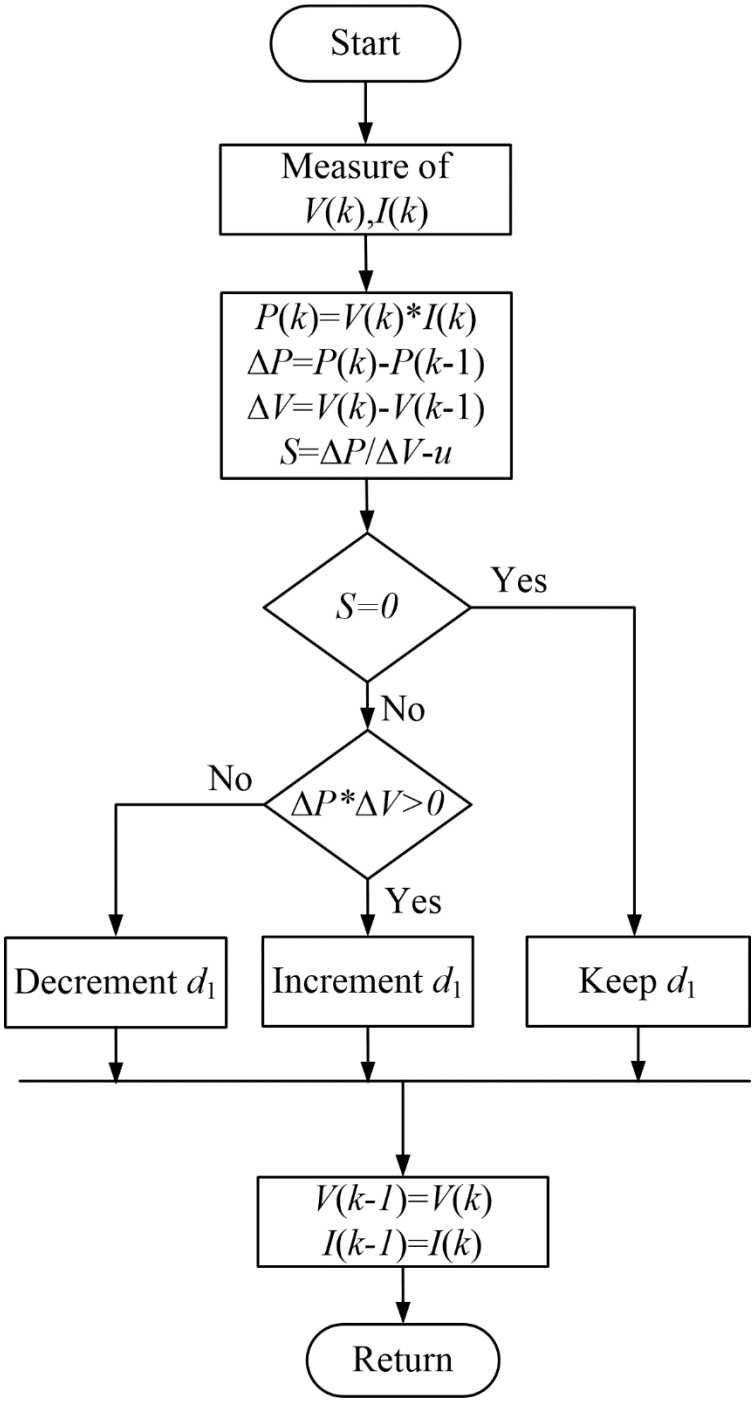

Fig. 4.2 The diagram of the MPPT.

The $\Delta P/\Delta V$ can be regulated by changing the duty cycle d_1, as shown in the Fig. 4.2. V (k), I (k) are the instantaneous value of the voltage and current of PV system. The parameter u is a small value (e.g.$2e^{-7}$) to ensure the slop $\Delta P/\Delta V$ is small enough to approach 0. From the P-V curve, the working point is in the left of the curve when $\Delta P*\Delta V>0$, and in the right when $\Delta P*\Delta V<0$. Then change the d_1 to control the trend of its working point until S<=0.

4.2 Control Strategy for Maximum Power Point Tracking of Wind Turbine

Similar to the PV system, wind turbine has a complex relationship between its operating environment and the maximum power they can produce. The following formula illustrates factors that are important to the performance of a wind turbine.

$$P = \frac{1}{2}\rho A v^3 C_p \tag{4.2}$$

Where ρ is the air density (kg/m^3), A is the turbine swept area (m^2), v is the wind speed (m/s), and C_p is the power coefficient of performance or rotor efficiency. And

$$A = \frac{1}{4}\pi D^2 \tag{4.3}$$

Where D is the wind turbine rotor diameter.

The value C_p is related to the tip speed ratio λ and pitch angle β represented as the formula (4.4). The ratio of tip speed (TSR) of wind turbine blade to wind velocity is defined as the formula (4.6). The graph of these three parameters is shown as Fig. 4.3, which is represented as C_P-λ curve. At $\lambda = 0$ the rotor does not rotate and hence cannot extract

power from the wind. At very high λ (here at λ=14) the rotor runs so fast that it is seen by the wind as a completely blocked disc, hence no possibility to extract energy from a moving mass (the wind). Somewhere between λ=0 and λ=14 there will be an optimum value (λ=8 in the picture) where the maximum power is extracted. According to the Betz Law, the maximal possible C_p can be 0.593, which means a maximum of 59.3% of the available wind power can be converted to mechanical power at ideal conditions, whatever the energy conversion device is. However, Real wind generators do not reach this theoretical optimum value. The power coefficient C_p obtains its maximum value only when the λ equals its optimal value λ_m.

$$C_p(\lambda,\beta) = C_1\left[\frac{C_2}{\lambda_i} - C_3\cdot\beta - C_4\right]e^{-\frac{C_5}{\lambda_i}} + C_6\lambda \tag{4.4}$$

With:

$$\frac{1}{\lambda_i} = \frac{1}{\lambda + 0.08\beta} - \frac{0.035}{\beta^3 + 1} \tag{4.5}$$

$$\lambda = \frac{\omega\cdot R}{v} \tag{4.6}$$

The coefficients C_1, C_2, C_3, C_4, C_5, and C_6 are shown in the table II. ω, R and v represent the rotor rotational speed in radians/second, the radius of the turbine and the wind velocity respectively.

TABLE II. The C_1, C_2, C_3, C_4, C_5, and C_6 value

Coefficients	C_1	C_2	C_3	C_4	C_5	C_6
Value	0.5176	116	0.4	5	21	0.0068

The characteristic curve of power of wind turbine, turbine speed and wind velocity are derived from C_P-λ curves shown in Fig. 4.4. Hence, if the turbine power and the rotor speed are known for any operating condition, the wind speed can be calculated. When the wind turbine is adjusted to its optimal value λ_m as well as the power coefficient C_P reaching its maximum $C_{P\max}$, the maximum power extraction is arrived.

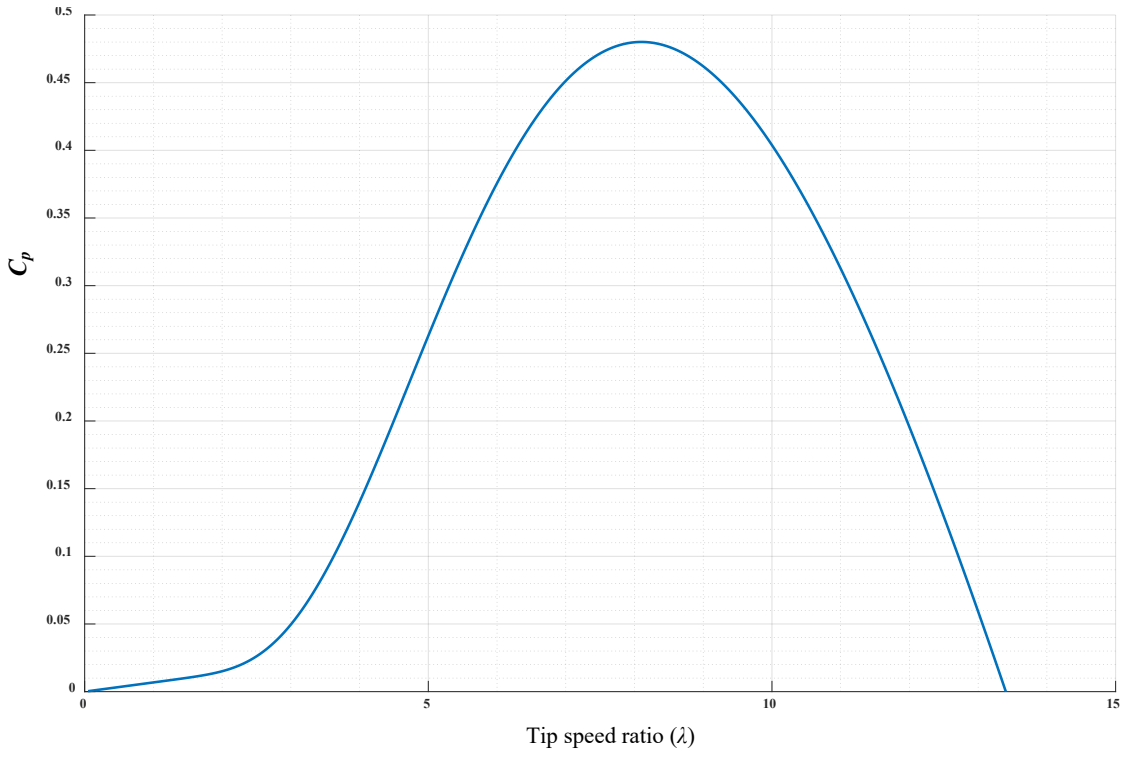

Fig. 4.3 C_P-λ curve.

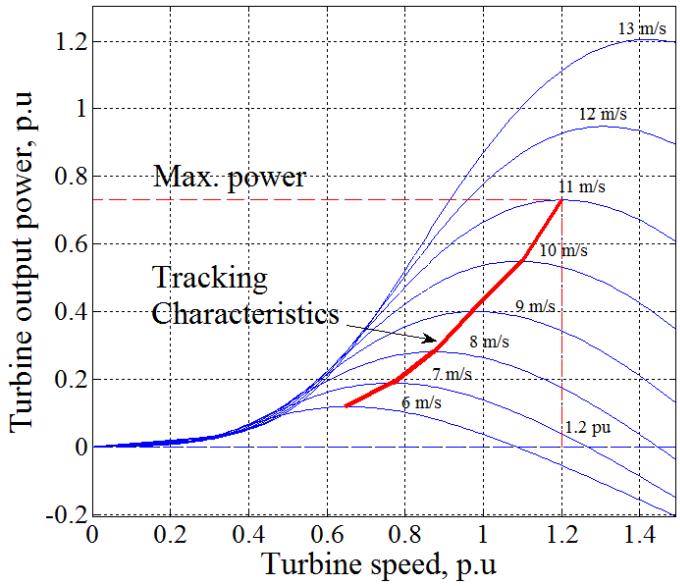

Fig. 4.4 Power-wind speed curve.

4.3 Simulation results

Fig. 4.5 shows the simulation results under the different scenarios. When t < 1 sec, the available renewable energy is low, Ports 1 and 2 work in the MPPT mode and the battery works in the discharge mode to supply power to the DC-link. At t = 1 s, renewable energy is more than the demand, the battery voltage reaches its maximum value, i.e., 30 V, the charge voltage is clamped to be 30 V and renewable energy sources do not work in the MPPT mode. At t = 2.5 s, renewable energy is not available, battery is discharged to supply the load. The reference DC link voltage, i.e., V^*_{dc}, is set as 183 V before t = 3.5 s, which indicates the converter works in the boost mode. After 3.5 s, v_{dc} is 177 V, the converter works in the buck mode since the battery current is positive. The result demonstrates the effective power management of the DC microgrid. TABLE III shows all the parameters for the converter.

TABLE II: Parameters of the Converter.

Leakage inductor	L_s	2 μH
Battery port filter inductor	L_b	10 μH
Battery port filter capacitor	C_b	100 μF
Switching frequency	f	100 kHz
Transformer turn ration	n	60: 12

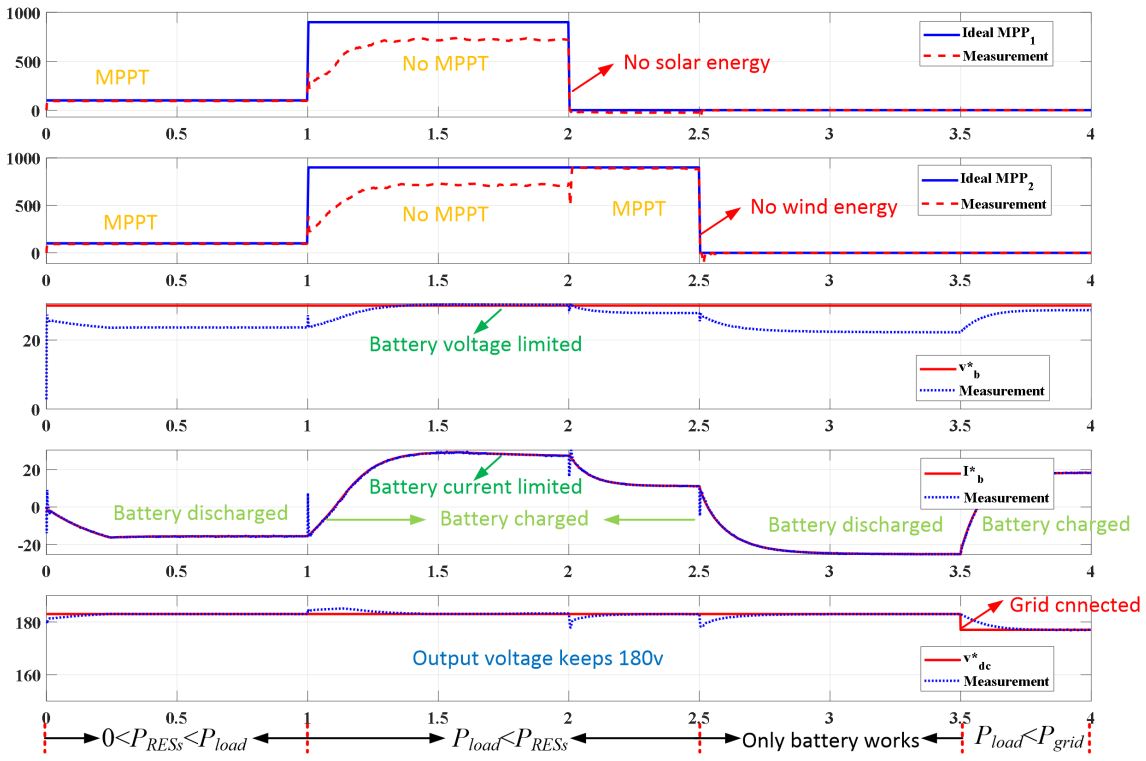

Fig. 4.5 Simulation result.

Chapter 5 : Experimental Demonstration and Validation

5.1 Experimental Setup

A 1 kW prototype was built to validate the proposed four-port DC-DC converter. Fig. 5.1 shows the overall experimental setup. The four-port DC-DC converter is connected to a BK PVS60085MR PV simulator, a DC voltage source is used to simulate the WTG. All real-time control algorithms are implemented in an eZdsp F28335 control board.

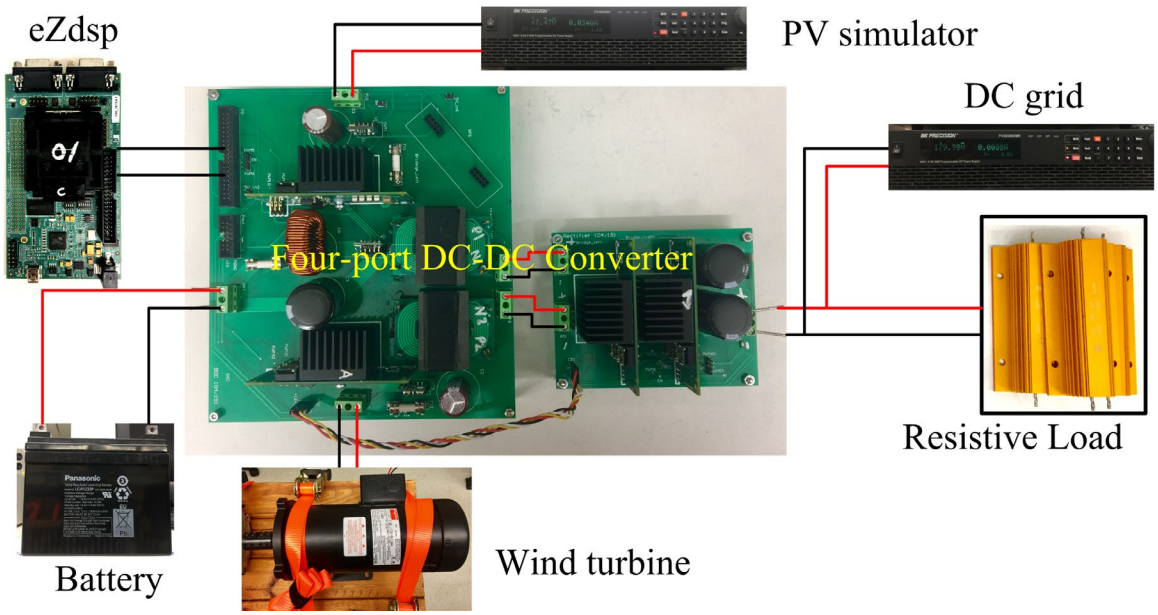

Fig. 5.1 Experimental setup.

5.2 Transformer Design and Calculation of Leakage Inductance

As an alternative to wire-wound transformers, which consist of each winding being wound on a separate soft iron limb or core, the planar transformer continues to emerge, making it ideal in certain application toward higher efficiency and performance along with miniaturization. A planar transformer is essentially a transformer that uses flat windings, usually on a PCB board, instead of copper wire to form the coils. The PCB construction

creates a different form factor that not only saves you space, time, and costs, but suits your needs uniquely and specifically. There are four types of “transformer construction” and designs available with the different order of the PCB board shown as Fig. 5.2. Case-*a* is a fully interleaved winding configuration; case-*b* and case-*c* are partially interleaved winding

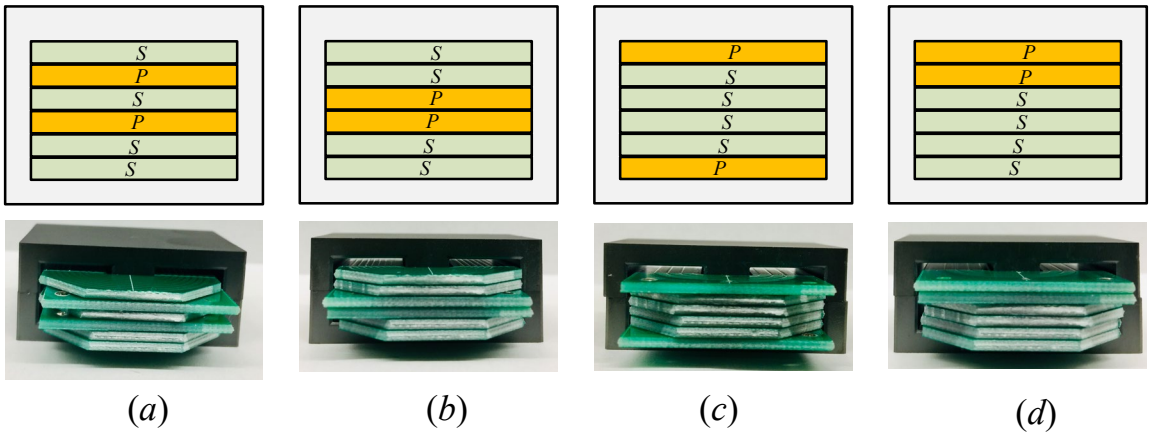

Fig. 5.2 Four winding configurations.

configuration; case-*d* is non-interleaved winding configurations. All these planar transformers consist of six PCB board, where six turns with two winding portion and fourteen turns with four winding portion are wound for the primary side and the secondary side, respectively, thus the theoretical turn ratio of the transformer is 4.67.

Leakage inductance is an inductive component present in a transformer that results from the imperfect magnetic linking of one winding to another. In an ideal transformer, 100% of the energy is magnetically coupled from the primary to the secondary windings. Imperfect coupling reduces the signal induced in the secondary windings. Any magnetic flux that does not link the primary winding to the secondary winding acts as inductive impedance in series with the primary, therefore this "leakage inductance" is shown on a

schematic diagram as an additional inductance before the primary of an ideal transformer shown as Fig. 5.3.

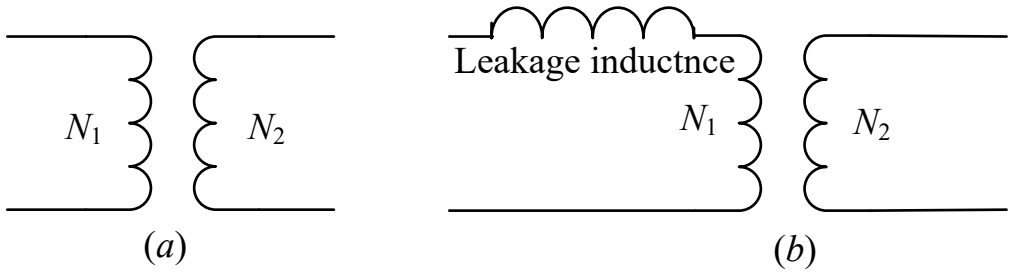

Fig. 5.3 (*a*) Ideal transformer (*b*) real transformer showing leakage inductance.

Leakage inductance should be low enough when it is undesirable in a wound component in some applications, but must be a greater proportion of the total inductance to provide an energy storage medium that is essential to achieve correct operation of the circuit design. It is therefore important that the value of leakage inductance of the transformer is known to be within specified limits. In certain transformer designs, the increased proportion of leakage inductance is usually achieved by introducing an air gap in the core design or using non-interleaved windings. The value of leakage inductance can be calculated by the waveform of i_{p1} shown as Fig. 5.4 . For the transformer, the differential equation can be deduced as follows:

$$\begin{cases} v_p = L_{s1}\dfrac{di_p}{dt} + v_T \\ n \cdot v_T = v_s \end{cases} \tag{5.1}$$

Thus

$$L_{s1} = \frac{v_{p1} - v_{s1}/n}{d_i/dt} \tag{5.2}$$

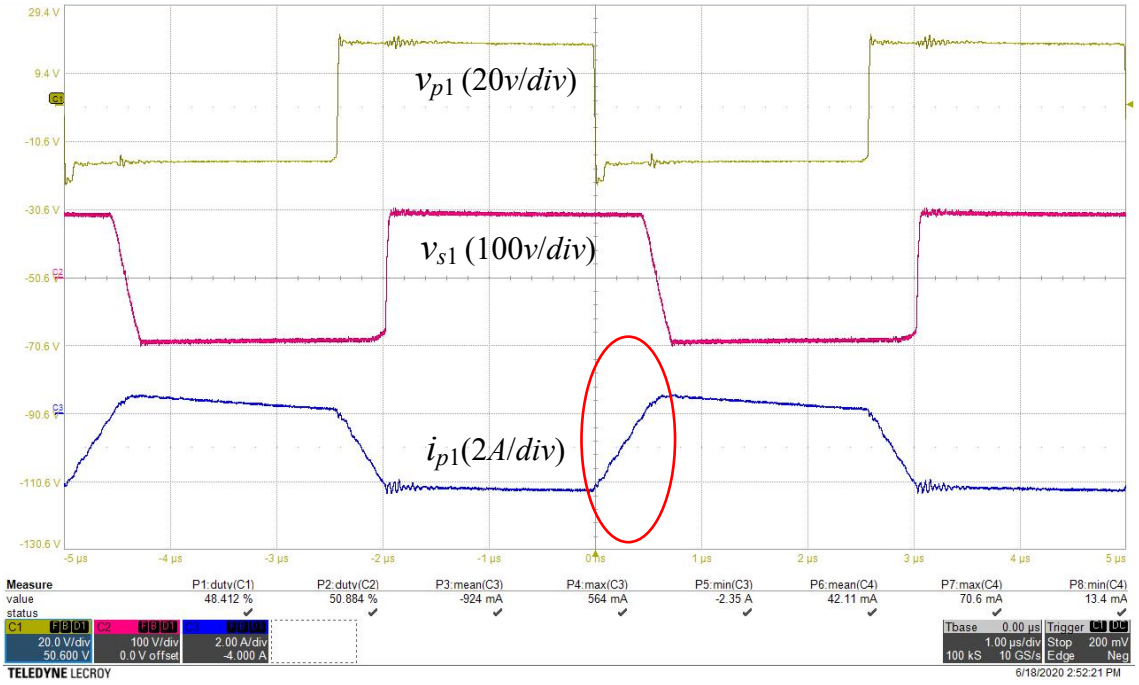

Fig. 5.4 The waveforms for calculation of the leakage inductance.

The leakage inductances and parameters for these four types of transformer construction are shown in the TABLE IV. The case-*d* non-interleaved winding configurations was used in the experiment.

TABLE IV: Parameters of the transformer

Leakage inductor of case-*a*	L_{s_a}	1.63 µH
Leakage inductor of case-*b*	L_{s_b}	2.3 µH
Leakage inductor of case-*c*	L_{s_c}	4.6 µH
Leakage inductor of case-*d*	L_{s_d}	6.4 µH
Transformer turn ration	*n*	56: 12
Core material	/	Ferrite Cores 98
Core initial permeability	/	2300

5.3 Steady-State Response and Power Curve of Prototype

Fig. 5.5 shows the measured steady-state waveforms of the currents i_{p1} and i_{dc} when the converter works in the boost mode. In this mode, a DC source is connected to the Port 4 to simulate the DC-microgrid. The WTG and PV panel are not connected to the converter. As shown in the picture, the phase shift between S_1 and S_5 is $\delta = 0.6$. When S_1 is off, i_{p1} increases; when S_1 is on, i_{p1} decreases, the measured i_{p1} well replicates the waveform shown in Fig.2.4. The mean value of i_{dc} is 0.435 A, which indicates the battery is discharged to supply the power to the DC-microgrid, therefore, the converter work in the boost mode. Fig. 5.6 shows the waveforms when δ = 0.4. As shown in Fig. 5.6, the mean value of i_{dc} is around – 0.742A, which means the battery is charged by the DC microgrid and the converter works in the buck mode. Therefore, the bidirectional power flow between the

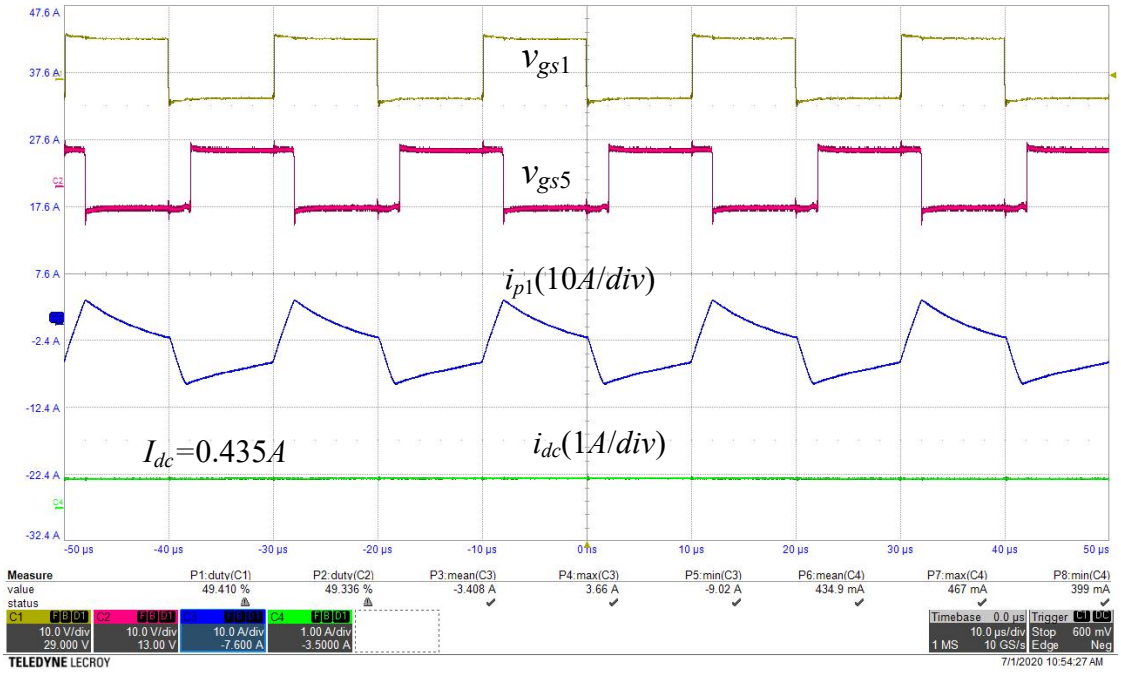

Fig. 5.5 Measured waveforms of v_{gs1}, v_{gs5}, i_{p1} and i_{dc} when δ= 0.6.

LVS and HVS can be achieved by the proposed converter which is suitable for the micro-grid.

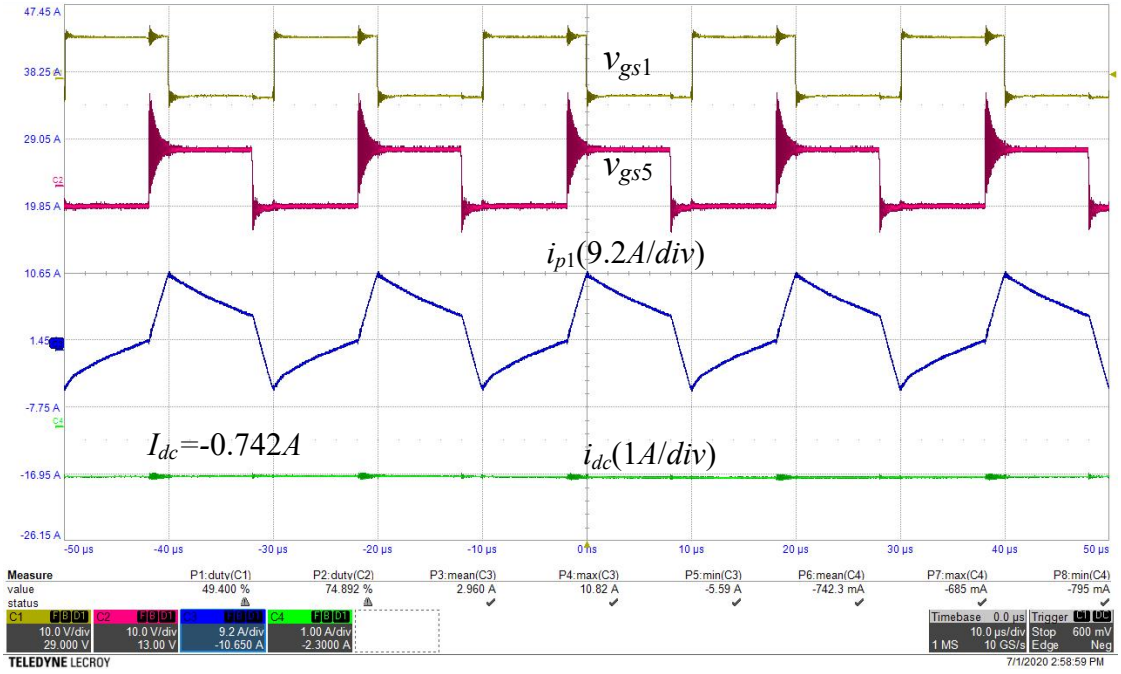

Fig. 5.6 Measured waveforms of v_{gs1}, v_{gs5}, i_{p1} and i_{dc} when δ= 0.4.

When power is transferred between the battery and DC macro-grid at different phase shift δ, the power curve has been given in Fig. 5.7. The graph's horizontal axis $\Delta\delta$ shows the relative phase shift between S_1 and S_5, which can be calculated by $\delta = \Delta\delta + 1/2$. The blue line P_c is the theoretical calculations of power. The orange and grey lines represent the experimental data of charged and discharged power through battery. It can be seen from the theoretical calculations and Experimental results that they have the satisfactory agreement with taking loss of efficiency into account. In addition, the battery is discharged when $\delta \in [0.5, 0.2]$, and charged when $\delta \in [0.3, 0.5]$, which is consistent with the theoretical analysis, thus verifying the correctness and effectiveness of the proposed prototype.

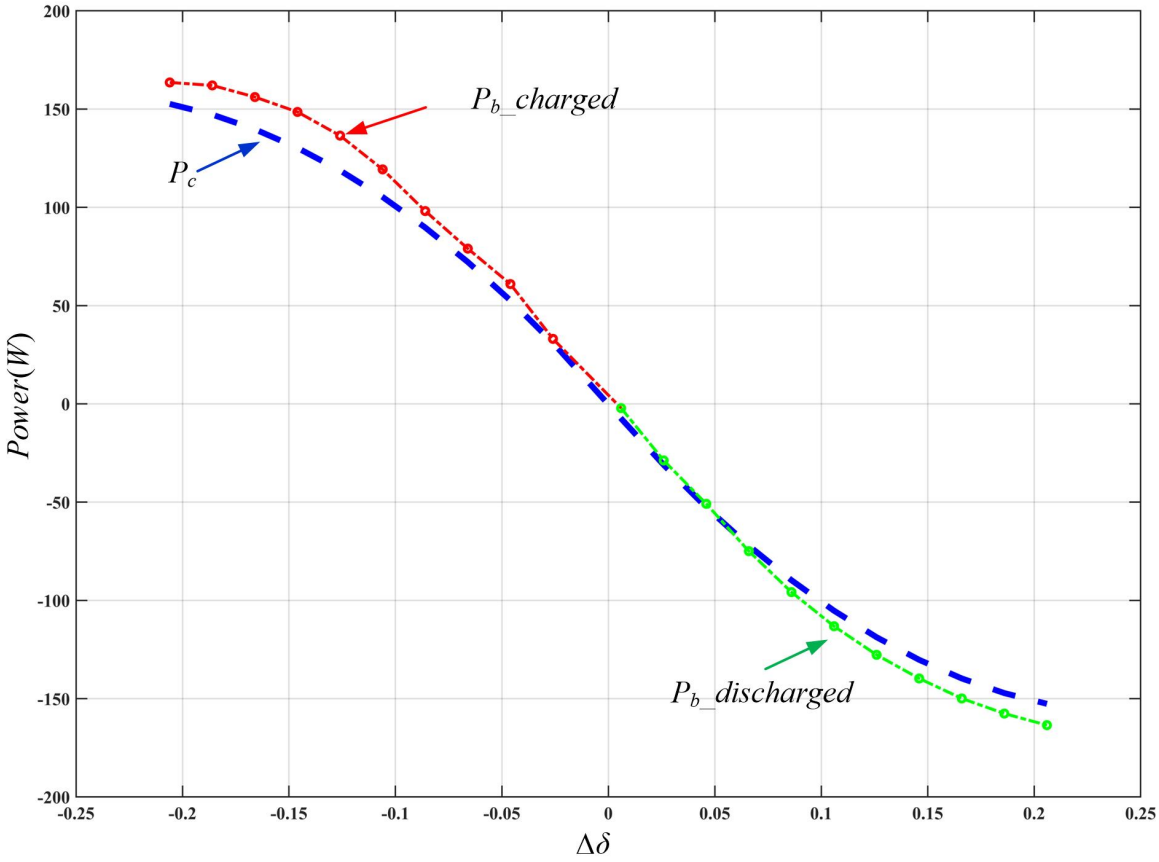

Fig. 5.7 Power curve of the porotype.

5.4 Dynamic Response of Prototype

Fig. 5.8 and Fig. 5.9 further show the step response when different port power is unavailable. As shown in Fig. 5.8, the converter is first connected to three sources and DC grid. The positive i_b indicates the battery works in the charge mode. At t = 0.42s, both WTG and solar panel are disconnected, i.e., P_{RES} = 0, i_b first drops to 0 A and then increases to 4A within 150 ms. According to i_{dc}, which changes from positive to negative, the converter is changed from the boost mode to the buck mode, indicating the capability of bidirectional energy management. During the whole transient period, the battery is capable of keeping the constant current to be 4A, which validates the effectiveness of controllers of the battery.

Fig. 5.9 shows the transient when DC microgrid is disconnected and reconnected to the converter. As shown in Fig. 5.9, when the DC voltage is removed, the operation mode of the battery quickly is switched from the charge mode to the discharge mode to regulate the DC link voltage, v_{dc} first drops and then increases to its reference value, which validates the effectiveness of G_{cib}(s) and G_{cvdc}(s). The solar power is maintained approximate 47 W which is close to its pre-defined the maximum power 50 W, which validate the effectiveness of MPPT controllers. When the DC microgrid is reconnected, the operation mode is changed from the discharge mode to the charge mode, again, the operation points of the PV panel are close to its MPP. During the whole transient, the dc-link voltage is controlled to be 180 V during the entire of the operation time due to the G_{cvdc} (s).

The voltage control maintain the value of v_{dc} even with the load variation, as shown in Fig. 5.10 . When the load changes from 500Ω to 300Ω, the status of battery changes from charge mode to discharge mode soon, which is controlled by the phase shift δ to realize bus voltage regulation. The solar power is consistent in the process, which shows the PV works in MPPT mode when transited between battery charge domain and battery discharge domain.

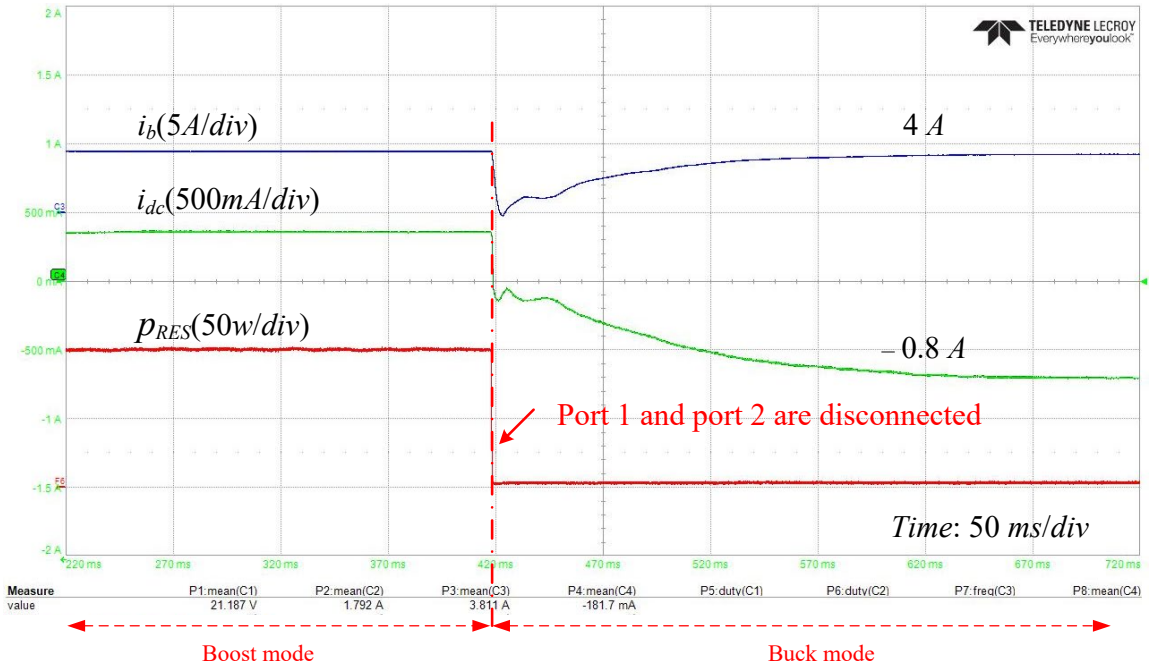

Fig. 5.8 Measured waveforms when Ports 1 and 2 are disconnected from the converter.

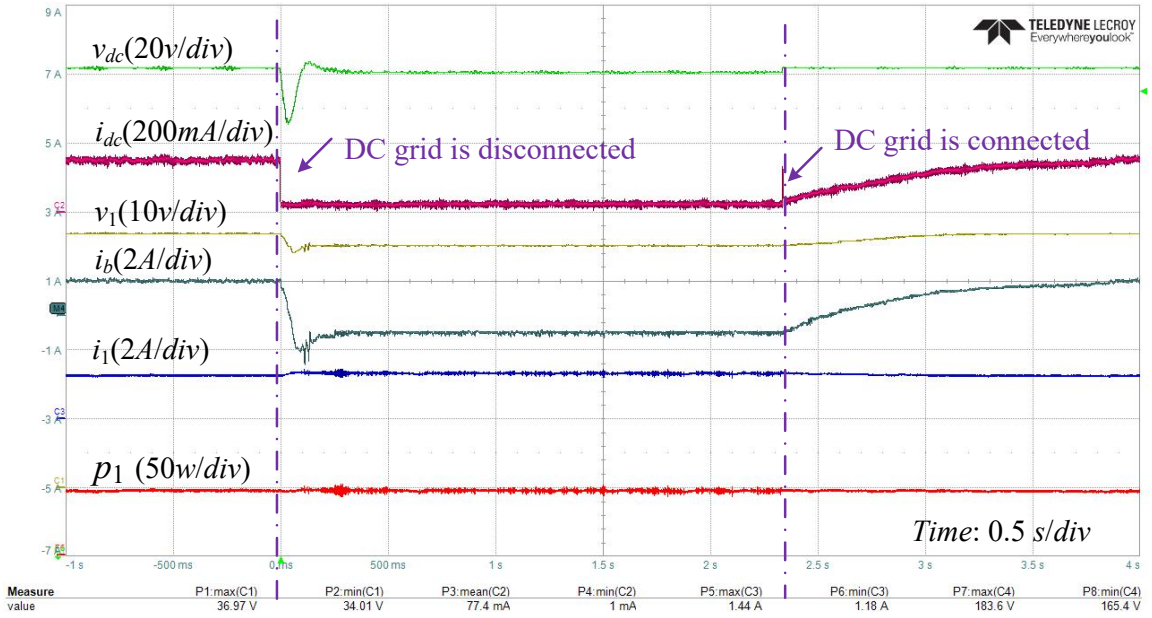

Fig. 5.9 Measured waveforms when DC microgrid is disconnected and reconnected to the converter.

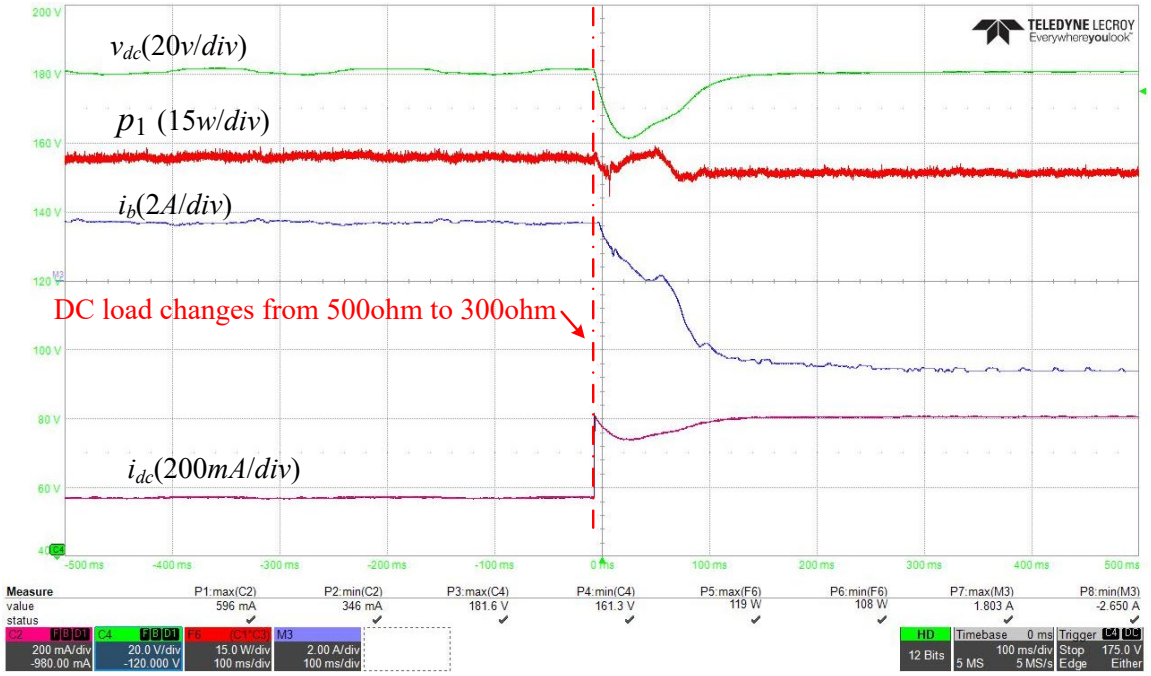

Fig. 5.10 Measured waveforms when DC load changes from 500Ω to 300Ω.

Chapter 6 : Conclusions, Contributions and Recommendations for Future Work

6.1 Conclusions and Contributions

This thesis presents a novel bidirectional four-port converter and its corresponding controllers design and power management for a hybrid wind, solar, battery, and DC micro-grid system. There are a lot of advantages listed as following:

- Cost-effective design: using the least number of switches while maintaining ZVS performance to minimize the power losses.
- Novel bidirectional power flow: the porotype can switch freely between boost mode and buck mode, and the battery can be charged by the RES or microgrid individually.
- High efficiency: RESs can achieve MPPT individually or simultaneously.

More specifically, three controllers were designed to control the voltage/current of the battery, and the output voltages of the converter respectively. The converter is capable of maximizing the energy efficiency by maintaining the MPPT of the renewable resource with dual energy transmission. Meanwhile, the seamless operation modes transition makes it possible to manage power flow at the system level. Finally, a prototype with180V main bus and 1kW output power has been built, and the effectiveness of the proposed topology, controllers and power management method has been verified by the simulation and experimental results with good steady-state and dynamic performances.

6.2 Recommendations for Future Work

Even though the proposed converter can lead the trend of the multiport converters, there are several problems unsolved, which motivates the future improvements of the existing controllers and integrated systems. Several possible and potential improvements are listed as followed.

- High frequency design: for converters with a soft-switching technique, the switching frequency can be increased to further decrease the size of the output capacitor and inductor to save board space while maintaining their performance.
- High efficiency design: the efficiency can be higher by improving the transformer and advanced-technology switch.
- Parallel operation of multiple multiport converters: In future homes and buildings, multiport converters will be widespread usage, thus each home or building will be a microgrid. How to connect them to the grid and unify the control operation management is critical.

Reference

[1] M. Liserre, T. Sauter, and J. Y. Hung, "Future energy systems: integrating renewable energy sources into the smart power grid through industrial electronics," *IEEE Ind. Electron. Magazine*, vol. 4, no. 1, pp. 18-37, Mar. 2010.

[2] F. Weschenfelder, G. Leite, A. Costa, O. Vilela, C. Ribeiro, A. Ochoa, and A. Araújo, "A review on the complementarity between grid-connected solar and wind power systems," *J. Cleaner Production*,vol. 257, June 2020.

[3] Z. Chen, Q. Liu, X. Xiao, N. Liu, and X. Yan, "Integrated mode and key issues of renewable energy sources and electric vehicles' charging and discharging facilities in microgrid," in *Proc. IEEE 2nd IET Renewable Power Generation Conf. (RPG 2013)*, Beijing, pp. 1-4, Sept. 2013.

[4] S. J. AL-Chlaihawi and A. G. Al-GIZI, "A survey of multiport converters used in renewable energy*," 2016 Int. Symposium on Fundamentals of Electrical Engineering (ISFEE)*, Bucharest, pp. 1-4, July 2016.

[5] D. Heide, L. Bremen, M. Greiner, C. Hoffmann, M. Speckmann, and S. Bofinger, "Seasonal optimal mix of wind and solar power in a future, highly renewable Europe," *Renewable Energy*, vol. 35, pp. 2483-2489, Nov. 2010.

[6] F. Blaabjerg and K. Ma, "Wind energy systems," *Proceedings of the IEEE*, vol. 105, no. 11, pp. 2116-2131, Nov. 2017.

[7] J. M. Carrasco et al., "Power-electronic systems for the grid integration of renewable energy sources: a survey," *IEEE tran. Ind. Electron.*, vol. 53, no. 4, pp. 1002-1016, June 2006.

[8] "Cost-reduction roadmap for residential solar photovoltaics (PV), 2017–2030," U.S. *Department of Energy. National Renewable Energy Laboratory*, 2018. (Available online: https://www.nrel.gov/docs/fy18osti/70748.pdf)

[9] "The evolving market structure of the U.S. residential solar PV installation industry, 2000-2016," U.S. *Department of Energy. National Renewable Energy Laboratory*, 2018. (Available online: https://www.nrel.gov/docs/fy18osti/70545.pdf)

[10] S. B. Kjaer, J. K. Pedersen and F. Blaabjerg, "A review of single-phase grid-connected inverters for photovoltaic modules," *IEEE Trans. Ind. Appl.*, vol. 41, no. 5, pp. 1292-1306, Sept.-Oct. 2005.

[11] M. S. Whittingham, "History, evolution, and future status of energy storage," *Proceedings of the IEEE*, vol. 100, no. Special Centennial Issue, pp. 1518-1534, May 2012.

[12] A. Khaligh and Z. Li, "Battery, ultracapacitor, fuel cell, and hybrid energy storage systems for electric, hybrid electric, fuel cell, and plug-in hybrid electric vehicles: State of the art," *IEEE Trans. Veh. Technol*., vol. 59, no. 6, pp. 2806-2814, July 2010.

[13] H. Weiss, T. Winkler, and H. Ziegerhofer, "Large lithium-ion battery-powered electric vehicles - From idea to reality," in *Proc. 2018 ELEKTRO*, Mikulov, pp. 1-5, May 2018.

[14] R. Fatima, A. A. Mir, A. K. Janjua, and H. A. Khalid, "Testing study of commercially available lithium-ion battery cell for electric vehicle," in *Proc. 2018 1st Int. Conf. on Power, Energy and Smart Grid (ICPESG)*, Mirpur Azad Kashmir, pp. 1-5, Apr. 2018.

[15] B. Dunn, H. Kamath, and J.-M. Tarascon, "Electrical energy storage for the grid: A battery of choices," *Science*, vol. 334, no. 6058, pp. 928–935, Nov. 2011.

[16] N. Rampersadh and I. E. Davidson, "Grid energy storage devices," in *Proc. 2017 IEEE PES PowerAfrica*, Accra, pp. 121-125, June 2017.

[17] N. Anku, J. Abayatcye, and S. Oguah, "Smart grid: An assessment of opportunities and challenges in its deployment in the ghana power system," in *Proc. 2013 IEEE PES Innovative Smart Grid Technologies Conf. (ISGT)*, Washington, DC, pp. 1-5, Feb. 2013.

[18] O. Egbue, D. Naidu and P. Peterson, "The role of microgrids in enhancing macrogrid resilience," *2016 Int. Conf. on Smart Grid and Clean Energy Technologies (ICSGCE)*, Chengdu, pp. 125-129, Oct. 2016.

[19] M. Zachar and P. Daoutidis, "Microgrid/Macrogrid energy exchange: a novel market structure and stochastic scheduling," *IEEE Trans. on Smart Grid*, vol. 8, no. 1, pp. 178-189, Jan. 2017.

[20] N. M. Nithin, K. Muhammedali Shafeeque and S. Sheik Mohammed, "A novel one stage buck-boost inverter," *2019 IEEE Int. Conf. on Intelligent Techniques in Control, Optimization and Signal Processing (INCOS),* Tamilnadu, India, pp. 1-4, Apr. 2019.

[21] A. Alassi, A. Al-Aswad, A. Gastli, L. B. Brahim and A. Massoud, "Assessment of isolated and non-isolated DC-DC converters for medium-voltage PV applications," *9th IEEE-GCC Conf. and Exhib. (GCCCE)*, Manama, pp. 1-6, May 2017.

[22] Y. Tran and D. Dujic, "A multiport isolated DC-DC converter," *IEEE Applied Power Electron. Conf. and Exposit. (APEC)*, Long Beach, CA, pp. 156-162, Mar. 2016.

[23] J. Zeng, W. Qiao and L. Qu, "An isolated three-port bidirectional DC–DC converter for photovoltaic systems with energy storage," *IEEE Trans. Ind. Appl.,* vol. 51, no. 4, pp. 3493-3503, July-Aug. 2015.

[24] K. Shreelekha and S. Arulmozhi, "Multiport isolated bidirectional DC-DC converter interfacing battery and supercapacitor for hybrid energy storage application," *2016 Int.*

Conf. on Electrical, Electronics, and Optimization Techniques (ICEEOT), Chennai,pp. 2763-2768, Mar. 2016.

[25] J. Zeng, W. Qiao and L. Qu, "An isolated multiport bidirectional DC-DC converter for PV-battery-DC microgrid applications," *IEEE Energy Convers. Congr. Exposit. (ECCE)*, Pittsburgh, PA, pp. 4978-4984, Sept. 2014.

[26] Y. Tran and D. Dujic, "A multiport medium voltage isolated DC-DC converter," *IECON 42nd Annual Conf. of the IEEE Ind. Electron. Society*, Florence, pp. 6983-6988, Oct. 2016.

[27] V. R. Teja, S. Srinivas and M. K. Mishra, "A three port high gain non-isolated DC-DC converter for photovoltaic applications," *IEEE Int. Conf. Ind. Technol.*, Taipei, pp. 251-256, Mar. 2016.

[28] Y. Sato, H. Nagata and M. Uno, "Non-isolated multi-port converter integrating PWM and phase-shift converters," *TENCON 2017 - 2017 IEEE Region 10 Conf.*, Penang, pp. 1097-1102, Nov. 2017.

Appendix A

The code of the 2-D view of power curve:

```
d1 = 0.5;
delta = 0.25:0.0001:0.75;
mid = d1;
id1 = find(delta < 0.5); delta1 = delta(id1); % charge
id2 = find(delta >= 0.5 & delta < d1); delta2 = delta(id2);
id3 = find(delta >= d1); delta3 = delta(id3);            % discharge

P1 = 6000*(-2*delta1.^2 - d1^2 + 2* d1*delta1 + d1/2);
P2 = 6000*(- d1^2 + 2* d1*delta2 -2*delta2 + d1/2 + 1/2);
P3 = 6000*(2*delta3.^2 + d1^2 - 2* d1*delta3 + d1/2 - 2*delta3 + 1/2);

plot(delta1,P1,'b.-',delta2,P2,'r.-',delta3,P3,'g--');
xlabel('\delta'); ylabel('Power(W)');

grid on;
legend(' d1=0.5,0.25<delta<0.5',' d1=0.5,0.5<delta<0.75');
h=legend(' d1=0.5,0.25<delta<0.5',' d1=0.5,0.5<delta<0.75');set(h,'Fontsize',10);
```

The code of the 3-D view of power curve:

```
 d = 0.5:0.02:0.8;
 P = [];
 x = []; y = [];
n = length(d);
for i = 1: n
d1 = d(i);
delta = 0.25:0.0001:0.75;
mid = d1;
id1 = find(delta < 0.5); delta1 = delta(id1); % charge
id2 = find(delta >= 0.5 & delta < d1); delta2 = delta(id2);
id3 = find (delta >= d1); delta3 = delta(id3);            % discharge
```

```
P1 = 10000*(-2*delta1.^2 - d1^2 + 2* d1*delta1 + d1/2);
   P2 = 10000*(- d1^2 + 2* d1*delta2 -2*delta2 + d1/2 + 1/2);
   P3 = 10000*(2*delta3.^2 + d1^2 - 2* d1*delta3 + d1/2 - 2*delta3 + 1/2);
   pp = [P1,P2,P3];

   x = [x; d1*ones(1,length(delta))];
   y = [y;delta];
   P = [P;pp];
end

mesh(x,y,P);
xlabel('d_1'); ylabel('\delta'); zlabel('Power');
hold on

indexX = x(:,1);
indexY = y(1,:);
constantP = 0;
len = length(indexX);

Ytemp = [];
for i =1:len

   index = find(abs(P(i,:)-constantP)<0.02);
   temp = polyfit(P(i,index),indexY(index),4);
   tempY = polyval(temp,constantP);
   Ytemp = [Ytemp, tempY];
end
% figure;
curveP = constantP*ones(1,16);
hold on
plot3(indexX,Ytemp,curveP,'r*-');
```

Appendix B

The code of the ZVS analysis:

```
Ls = 6.4e-6; fs = 50e3; T = 1/fs; n = 5; Coss = 68e-12; Zr = sqrt(Ls/Coss); Vb = 18;
Vdc = 180; VT = Vdc/ (2*n);
w2 = 1/sqrt (n^2*Ls*Coss); dt1 = pi*sqrt(Ls*Coss);
delta = 0:0.001:0.08;
d12 = 0.5;
Pc = VT*(Vb-0.5)./d12./( fs * Ls).*delta.*(0.5-abs(delta)); % Pc: calculated
Pc = Pc /0.85;                  % efficiency
Pb = Pc; Ib = Pb/Vb; Ib = Pb/(Vb - 0.16*Ib);

I2 = 0.5*(Ib + (Vb-VT)/(2*Ls*fs) + 2*VT*abs(delta)/( Ls * fs));
Ic = 2*sqrt(VT*Vb)/Zr;
m = length(delta); ZVS2 = zeros(m,1); ZVS5 = ZVS2;
Idx2 = find(I2 > Ic); ZVS2(Idx2) = 1;
dt = max(Ls *I2/(Vb + VT),0);
tr2 = acos(1 - VT/Vb )/w2;
dm = (dt + tr2)/T;
Idx5 = find(delta >= dm);ZVS5(Idx5) = 2;

delta2 = delta(Idx2); P2 = Pb(Idx2);
delta5 = delta(Idx5); P5 = Pc(Idx5);

plot(delta*100,Pc,'b-'); hold on; stem(delta5*100,P5,'ro-');
legend('Power Curve','ZVS5');grid on;
xlabel('\Delta\delta (%)'); ylabel('Power (W)')
return;
```

Appendix C

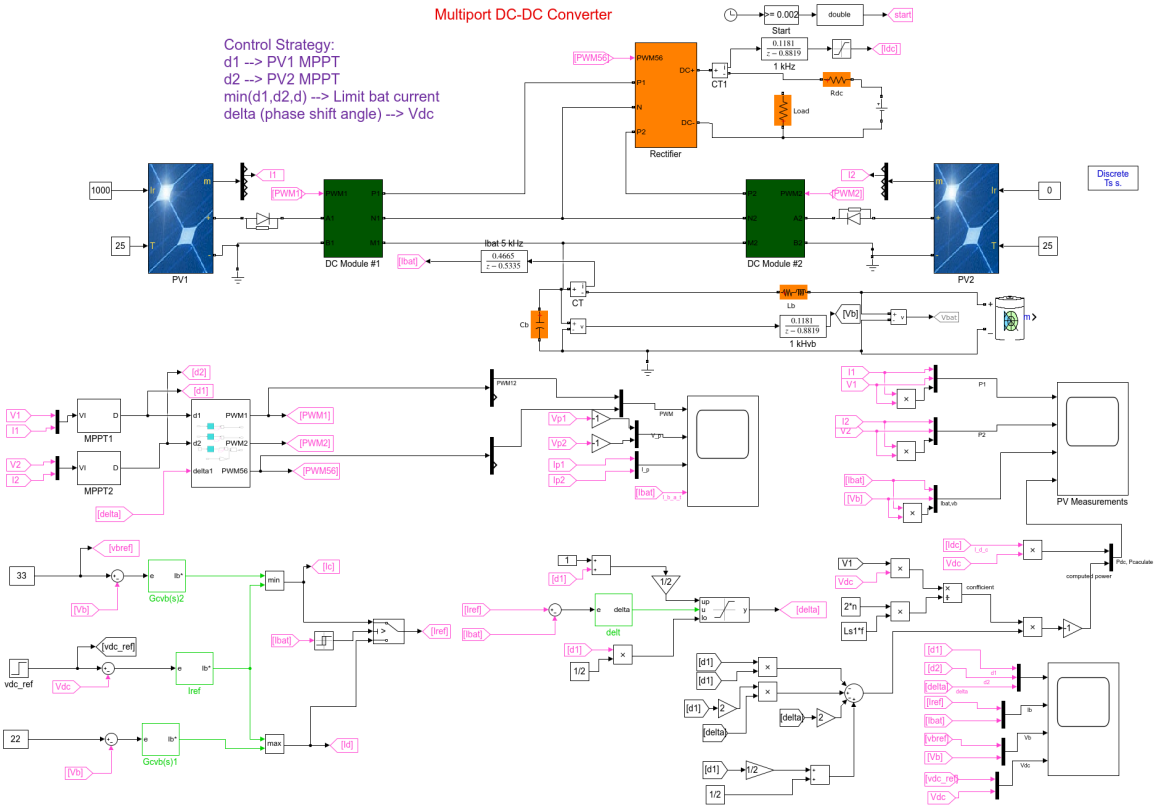

Figure 1. Simulation code

Appendix D

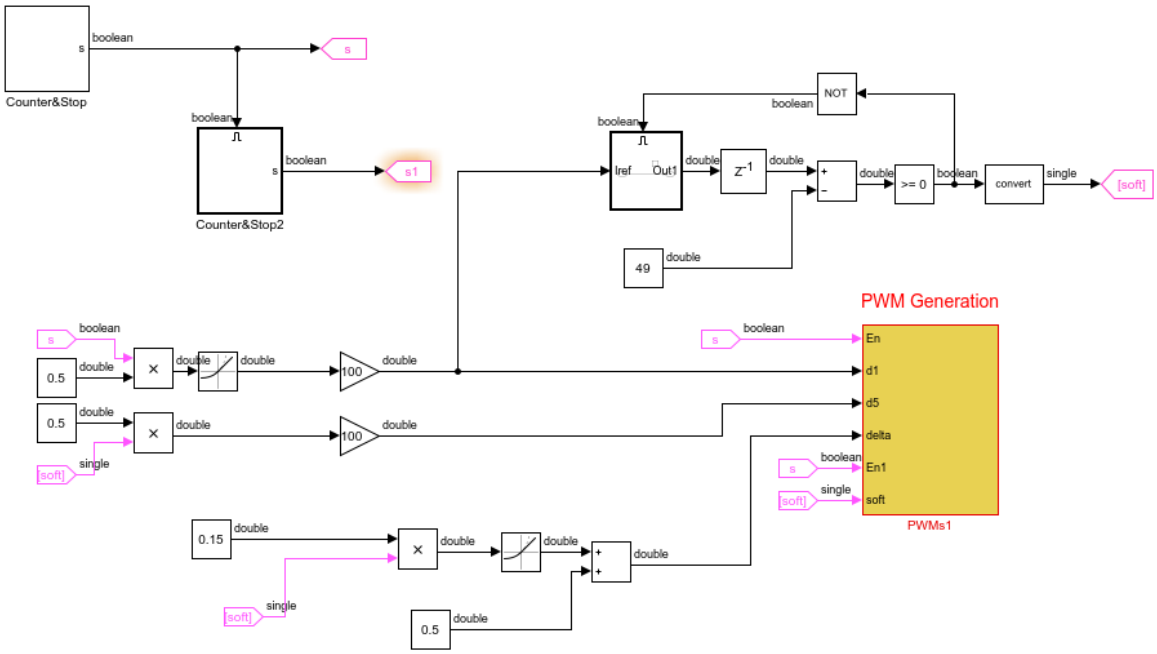

Figure 2. Experimental code

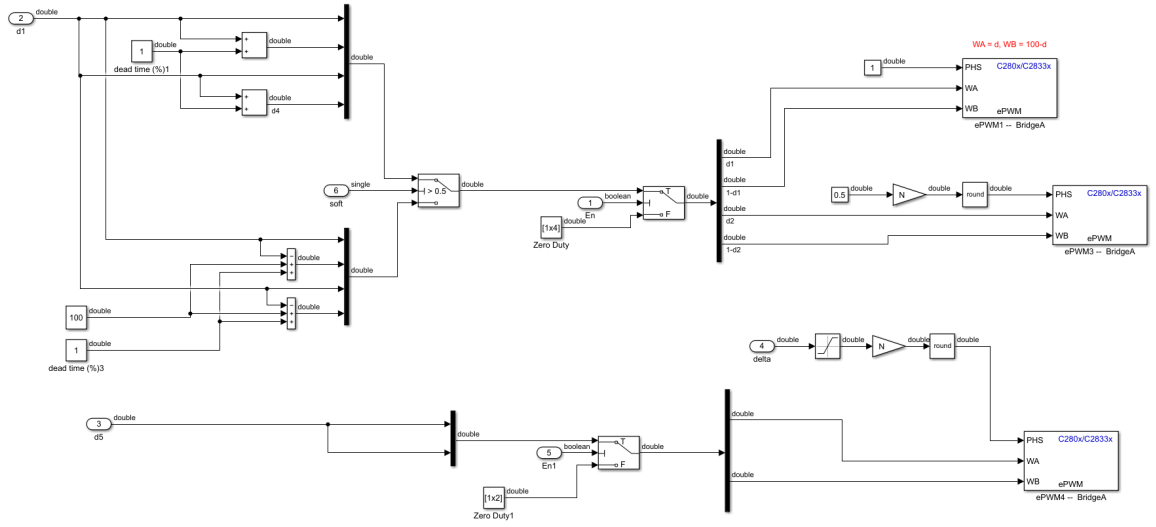

Figure 3. The code for soft start